JOURNAL OF SPACECRAFT AND ROCKETS
Vol. 60, No. 4, July–August 2023

Methods to Detect Impact-Induced Orbit Perturbations Using Spacecraft Navigation Data

Anne Aryadne Bennett*
University of Colorado Boulder, Boulder, Colorado 80303
Russell Carpenter†
NASA Goddard Space Flight Center, Greenbelt, Maryland 20771
and
Hanspeter Schaub‡
University of Colorado Boulder, Boulder, Colorado 80303

https://doi.org/10.2514/1.A35495

Debris strikes on operational spacecraft are becoming more common due to increasing numbers of space objects. Sample return missions indicate hundreds of minor strikes, but rigorous analysis is often only performed when a strike causes an anomaly in spacecraft performance. Developing techniques to identify and assess minor strikes that do not immediately cause anomalous behavior can help to validate models for debris populations and aid in the attribution of future anomalies. This study develops methods to detect subtle abrupt orbit perturbations indicative of minor debris strikes. An extended Kalman filter with dynamic model compensation is used to estimate a spacecraft's orbit state based on simulated full-state (i.e., GPS) measurements. The filter is applied to the data forward and backward in time, and then a modified Fraser–Potter smoother is used to produce a fused state estimate. Various test statistics are developed and compared to identify abrupt unexpected changes in spacecraft velocity; techniques include McReynold's filter-smoother consistency test and the Mahalanobis distance between forward and backward filter states. A trade study is performed to investigate the performance of test statistics as a function of filter parameters, and a Monte Carlo analysis illustrates the filter's ability to detect and estimate strikes.

Nomenclature

A, C_D, ρ, J_3	=	various common parameters for orbit perturbations, defined in accordance with referenced sources
$\boldsymbol{A}$	=	state dynamics Jacobian (units vary)
a, $\boldsymbol{e}$, $\boldsymbol{h}$	=	semimajor axis (km), eccentricity (unitless), and orbit angular momentum (km^2/s)
$\boldsymbol{a}$	=	spacecraft acceleration, km/s^2
$\boldsymbol{B}$	=	matrix that maps accelerations to state, unitless (for this application)
D_{MH}	=	Mahalanobis distance, unitless
$\tilde{\boldsymbol{H}}$	=	measurement partials, unitless (for this application)
$\boldsymbol{K}$	=	Kalman gain (units vary in accordance with measurement/state units)
m_d	=	mass of debris, kg
m_s	=	mass of spacecraft, kg
$\boldsymbol{P}$	=	covariance matrix ($\bar{\boldsymbol{P}}$ denotes *a priori*)
$\boldsymbol{Q}$	=	process noise spectral density matrix, km/s^2
q	=	process noise power spectral density, km^2/s^5
R	=	McReynold's filter-smoother consistency statistic
$\boldsymbol{R}$	=	measurement noise covariance (units vary in accordance with measurement units)
$\boldsymbol{r}$	=	spacecraft position, km (r denotes scalar position)
$\boldsymbol{S}$	=	process noise covariance (units vary in accordance with state units)
$\boldsymbol{v}$	=	spacecraft velocity, km/s (v denotes scalar velocity)
$\boldsymbol{v}_d$	=	velocity of debris, km/s
$\boldsymbol{W}$	=	weighting function for smoother, unitless
$\boldsymbol{w}$	=	unmodeled acceleration, km/s^2 ($\dot{\boldsymbol{w}}$ denotes time derivative)
X, Y, Z	=	components of $\boldsymbol{r}$ in inertial frame, km
$\boldsymbol{X}$	=	filter state, km, km/s, and km/s^2 ($\dot{\boldsymbol{X}}$ denotes time derivative)
β	=	momentum enhancement factor, unitless
γ	=	coefficients for calculating state process noise (units vary in accordance with state units)
$\Delta\boldsymbol{p}$	=	change in momentum of spacecraft, kg·km/s
$\Delta\boldsymbol{V}$	=	change in velocity of spacecraft, km/s
δ	=	Dirac delta
η	=	random element of first-order Gauss–Markov process, km/s^3
μ	=	geocentric gravitational constant, km^3/s^2
τ	=	time constant for first-order Gauss–Markov process, s
$\boldsymbol{\Phi}$	=	state transition matrix
$\sim\mathcal{N}(a, b)$	=	distributed according to Gaussian distribution with mean a and variance b

Received 22 June 2022; revision received 7 November 2022; accepted for publication 11 December 2022; published online 12 May 2023.

*Colorado Center for Astrodynamics Research, Autonomous Vehicle Systems Lab, 3775 Discovery Drive; also Mission Systems Engineer, Northrop Grumman Space Systems, 45101 Warp Drive, Dulles, Virginia 20166; anne.a.bennett@colorado.edu. Student Member AIAA (Corresponding Author).

†Deputy Program Manager/Technical, Space Science Mission Operations. Fellow AIAA.

‡Professor, Smead Aerospace Engineering Sciences Department, Autonomous Vehicle Systems Lab, 3775 Discovery Drive. Fellow AIAA.

I. Introduction

THE population of trackable fragmentation debris has more than doubled in the past 25 years [1]. This is especially concerning because while trackable debris can be avoided by maneuverable satellites, most fragmentation events also create clouds of debris too small to track. The Space Surveillance Network (SSN) tracks debris down to around 10 cm in low Earth orbit (LEO) and 70 cm in geosynchronous Earth orbit (GEO) [2], but a piece of debris smaller than 1 cm can cause mission-ending damage to a spacecraft if it hits a sensitive component [3], as shown in Fig. 1a. Based on current estimates for nontrackable debris populations, it is predicted that well under 10% of the potentially hazardous debris population is tracked [4]. While definitive anomaly attribution is challenging,

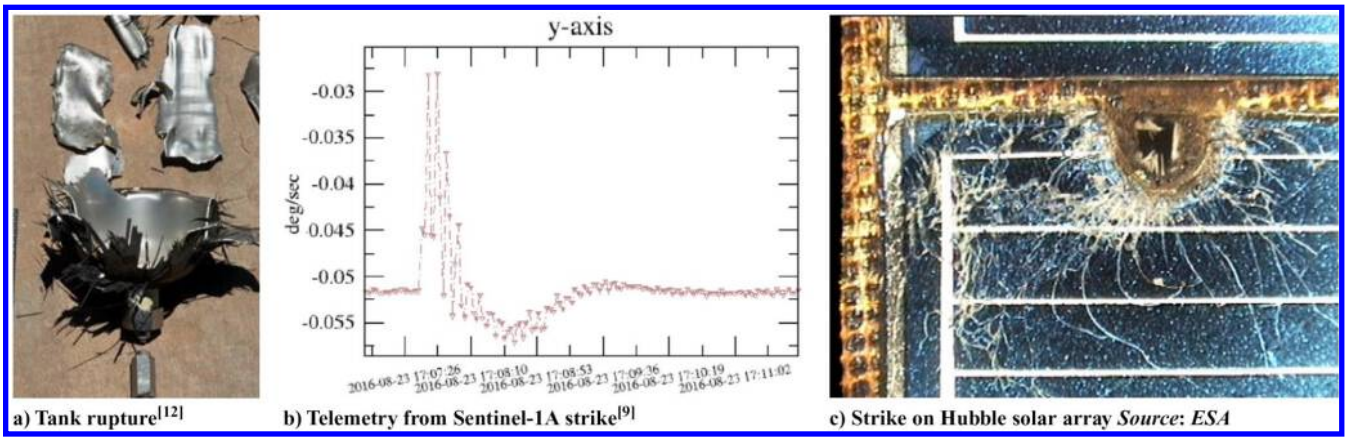

Fig. 1 Examples of small debris impact effects. The tank in a) was impacted by a 2 mm aluminum sphere. The hole in c) is 2.5 mm.

several spacecraft have experienced abrupt anomalous events plausibly caused by debris, such as Telkom-1 [5], AMOS-5 [6], NSS-806 [7], and Intelsat-29e [8].

However, not all debris strikes are fatal. In August of 2016, the Sentinel-1A spacecraft experienced an anomaly consisting of an abrupt attitude perturbation (Fig. 1b) coupled with a slight orbit change and simultaneous decrease in solar power output. Onboard cameras confirmed a debris strike on the solar array, but the damage was limited and operations continued nominally [9]. Similar events have been detected on NASA's magnetospheric multiscale (MMS) spacecraft, where anomalous behaviors have been noticed and attributed to strikes, but the effects were recoverable and operations continued nominally [10]. In addition to these damaging strikes, which cause anomalous behaviors, small strikes occur on spacecraft without even perturbing operations. Sample return missions such as the Long Duration Exposure Facility and the Hubble solar arrays have cataloged hundreds to thousands of debris craters after a few years on orbit (Fig. 1c) [11].

Other constellations have experienced events like Sentinel-1A, and a 2017 report by the NASA Engineering and Safety Center (NESC) incorporates these events into a study comparing observed anomalies to failures predicted using then-current debris models (ORDEM3.0) and typical risk assessment methods. The NESC report assessed reported versus predicted failures for several LEO satellite systems. For one LEO constellation, seven perturbation events had been observed where satellites experienced sudden unexpected movements thought to be caused by debris, while the risk assessment process predicted 24–164 perturbations. Comparing these and other events to predicted events, the NESC report found very low correlation between the on-orbit events and the ORDEM3.0 predictions, with ORDEM3.0 predicting a higher risk of failures and perturbations than these LEO systems have experienced [13]. A key recommendation of the NESC report is to collect data on satellite orbital perturbations and momentum changes.

The NESC report findings are timely, as the space industry is in a period of rapid change. The number of active spacecraft has more than doubled in the past 4 years. This burgeoning population leads to elevated concerns about space debris risks, with more objects potentially being hit by nontrackable debris, which creates still more debris. Meanwhile debris mitigation requirements for missions are spotty and sometimes archaic, with a smorgasbord of differing guidelines from various players. Against this backdrop it is imperative that models accurately assess risks and are consistent with operator experience to incentivize sustainable behaviors. Inaccurate risk assessments cast doubt on the state of debris, leading to a lack of consensus in the debris research community, which produces more-or-less stagnate policy and legislation with extremely limited progress on remediation. Accurate models are necessary so that the current status of debris is known and validated, enabling accurate, trusted predictions of the future debris environment and thus motivating effective legislation, policy, and remediation activities.

A silver lining emerges in the form of satellite-as-a-sensor initiatives. Following the NESC report's recommendation, these proliferated satellites themselves can be used as *in situ* sensing platforms to improve knowledge about the local debris environment. This can be accomplished by sensing the momentum perturbations produced by minor debris strikes and using the data to tune debris environment and risk models, refining estimates of uncertain parameters. In addition, detection of debris strikes has obvious implications for autonomous satellite state of health monitoring. While various dedicated sensors have been proposed to detect strikes, most satellites, especially low-cost commercial satellites, do not have the design bandwidth to fly these sensors. A preferred solution is developing methods to process standard telemetry used by many operational spacecraft to produce algorithms that can detect minor momentum perturbations too subtle to be observed in the normal course of operations.

This paper develops techniques to accomplish this by designing an orbit determination filter that accentuates abrupt, unexpected changes in spacecraft velocity. By postprocessing existing data or analyzing new data operators and modelers can gain information about the local debris environment for improved understanding of spacecraft risks. The goal of these techniques is to detect benign impacts that do not cause meaningful damage to a spacecraft, but could cause issues if impacting a sensitive component like a sensor, a battery, or a pressurant tank.

Various researchers have investigated similar concepts for identifying effects from abrupt, unexpected momentum transfer. Some key related work has been done by ExoAnalytic Solutions on detecting momentum impulse transfer events (MITEs) on GEO objects using their global telescope network. They have demonstrated a capability to detect orbit perturbations with in-track velocity changes of 0.2–10 mm/s [14]. Figure 2 shows an example of one MITE, as indicated by the measurement residuals from ExoAnalytic's ground-based network, where modeling a small ΔV resulted in an improved

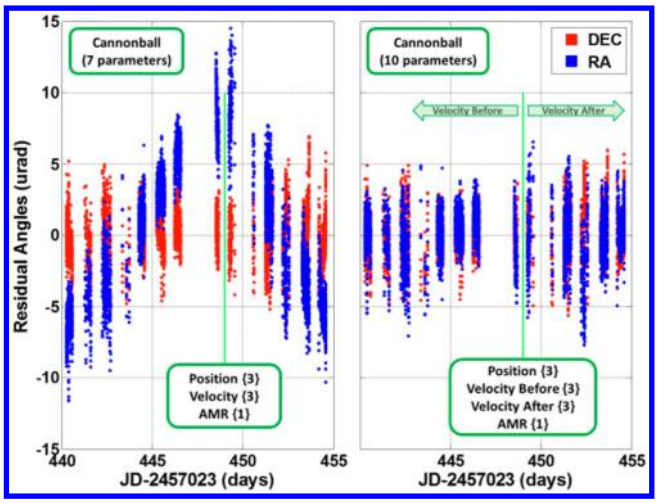

Fig. 2 Graphic published by ExoAnalytic Solutions [14] showing filter residuals with and without an estimated MITE.

fit for the residuals. Similarly, a recent study by the Fraunhofer Ernst-Mach-Institut assesses the momentum transferred during small hypervelocity impacts on spacecraft materials via modeling and test, and then simulates the dynamic response of a spacecraft to these disturbances [15]. On the LISA Pathfinder, located around L1, mission data was used to identify 54 micrometeoroid impact events [16] via rotational momentum transfer. A paper by the Institute for Defense Analyses discusses methods to monitor satellites for small changes in orbit [17] with the intent of cataloging minor debris impacts and feeding back the results to debris models. Methods proposed for detecting orbit changes include changes to satellite mean altitude (dSMA), crosslink disruption, and using standalone GPS position measurements to identify a discrepancy from the satellite's nominal orbit. Motivated by the NESC report, Bennett et al. developed methods to identify subtle perturbations in spacecraft angular momentum [18] and applied these techniques to NASA spacecraft [19], successfully identifying instances of unexpected abrupt angular momentum perturbations. This work is unique among these developments by implementing adaptations to a Kalman filter that uses typical navigation telemetry to enhance detectability of minor unexpected orbit changes.

Looking more broadly at orbit change detection, many authors have applied a broad smorgasbord of techniques for detecting unknown maneuvers using various filtering techniques. Highlights include the Orbit Determination Toolkit by Analytical Graphics, Inc., which employs a backward-running fixed-interval smoother to estimate velocity changes due to an impulsive maneuver [20], and various flavors of fixed-epoch smoother. Ko and Scheeres investigate the use of thrust Fourier coefficients to detect unknown maneuvers [21], while Holzinger et al. detect and characterize maneuvers using control-distance metrics [22]. Kelecy and Jah develop techniques to detect and reconstruct maneuvers of low-thrust LEO satellites [23], and Jiang et al. employ a Mahalanobis distance-based technique to detect unknown maneuvers [24].

This paper investigates a technique that is similar to but unique from these, wherein an extended Kalman filter (EKF) with dynamic model compensation (DMC) is used to estimate unmodeled accelerations as a first-order Gauss–Markov (FOGM) process and then augmented with various test statistics. The filter is applied forward and backward across the data and then smoothed, and various test statistics are developed and compared to identify the highest signal-to-noise ratios (SNRs) in the presence of a small change in velocity. The backward filter employs a mirrored FOGM model for the unmodeled accelerations and produces a state estimate using only "future" data, instead of a smoothed state estimate using both past and future data as with many smoothers. This modification enhances debris strike detectability by accentuating the difference between forward and backward states at the point of the debris strike. Simulated onboard navigation telemetry is employed to develop and test the filter; very basic orbit propagation and measurement noise models are used since the focus is on methods development and characterization.

First, a filter is developed to produce a state estimate appropriate for detecting orbit perturbations due to debris strikes. A "truth" orbit is generated using basic orbit propagation plus a simulated debris strike, and then this truth state is used to produce simulated GPS telemetry (position and velocity). An EKF with DMC is developed and applied to this telemetry, where the DMC models the acceleration state as an FOGM process. For debris strike detection the filter is modified such that it can be applied backward in time, and then a smoother is applied to fuse the forward and backward state into a smoothed state estimate. Several test statistics are developed to postprocess the filter output and accentuate the effects of the debris strike, including a Mahalanobis distance and a McReynold's filter-smoother consistency test. The filter performance is assessed using a trade study to characterize the filter's ability to detect strikes while trading the FOGM time constant and the power spectral density of the state process noise. A Monte Carlo analysis is performed to characterize the performance when detecting and estimating the size of a randomized debris strike. Finally, some minor orbit perturbations are added to the truth state but not the filter dynamics model. This illustrates the filter's performance in the presence of additional unmodeled accelerations. Discussion includes expected challenges when the filter is applied to on-orbit telemetry, and the potential utility of these techniques for understanding the hazardous nontrackable debris environment.

II. Filter Development

A. Generating Simulated Navigation Telemetry

Simple two-body orbit propagation is used throughout this paper, except as noted in Sec. IV.D. While modeling higher-order orbital perturbations will be critical in applying these techniques to on-orbit telemetry tools already exist for precision orbit determination and these tools can be leveraged in real-world applications. The focus here is on methods development, so a two-body orbit propagator is used. Default orbit parameters are listed in Appendix A; these are used throughout unless otherwise specified in the text.

A debris strike is applied as an instantaneous change in velocity ($\Delta \boldsymbol{V}$). Since the momentum transfer effects of a hypervelocity impact typically resolve in less than a second [25], a strike will essentially occur between two telemetry points. The momentum imparted by the debris strike is calculated as

$$\Delta \boldsymbol{p} = \beta m_d \boldsymbol{v}_d \tag{1}$$

where $\Delta \boldsymbol{p}$ is the momentum transferred to the spacecraft, β is the momentum enhancement factor [26], m_d is the mass of the debris, and $\boldsymbol{v}_d$ is the velocity of the debris relative to the spacecraft. This is applied in the inertial frame to produce the $\Delta \boldsymbol{V}$, but $\boldsymbol{v}_d$ can be specified in either the inertial or orbit frame and then converted if needed. By conservation of momentum, the change in spacecraft velocity is then

$$\Delta \boldsymbol{V} = \frac{\Delta \boldsymbol{p}}{m_s} \tag{2}$$

At the specified strike time this change in velocity is applied to the spacecraft state and the new poststrike orbit state is propagated for the rest of the specified simulation time. The default values for the debris strike parameters are provided in Appendix A, and any changes from these values are specified. Note that when a change is specified in the text as a scaled proportion to the "default" strike, the mass is scaled by that amount. The default debris mass is 0.2 g, so a "5X strike" specified in the text means that the mass of the debris is set to 1 g instead. From the spacecraft orbit state, full-state measurements are derived, intended as a basic simulation of GPS telemetry. These position and velocity measurements consist of the truth state with Gaussian noise superimposed in accordance with the noise parameters specified in Appendix A. As with orbit propagation this model is far simpler than real-world noise characteristics, comments on applying these methods to real-world telemetry are included in the discussion, Sec. V.

B. Implementing EKF with DMC

The EKF is implemented per the algorithm of Tapley, Schutz, and Born (TSB; [27], p. 212). The filter uses DMC, estimating unmodeled accelerations as part of the filter state. Thus the state vector consists of position $\boldsymbol{r}$, velocity $\boldsymbol{v}$, and unmodeled accelerations $\boldsymbol{w}$. With position and velocity measurements the measurement partials, $\tilde{\boldsymbol{H}}$, are straightforward:

$$\tilde{\boldsymbol{H}}_i = [\, \boldsymbol{I}_{6\times 6} \quad \boldsymbol{0}_{6\times 3} \,] \tag{3}$$

where $\tilde{\boldsymbol{H}}$ is defined and used per the TSB formulation, $\boldsymbol{I}_{6\times 6}$ is a 6×6 identity matrix, and $\boldsymbol{0}_{6\times 3}$ is a matrix of zeros. The covariance of the measurement noise (the $\boldsymbol{R}$ matrix per TSB notation) is provided in Appendix A.

The truth orbit is propagated with MATLAB's ODE45 function, but within the filter the state is propagated with a fourth-order Runge–Kutta (RK4) and the state transition matrix (STM) is propagated with

a second-order Runge–Kutta (RK2), in accordance with typical practices. Propagating the state and STM both with ODE45 also works as well but is significantly slower, while propagating the state with an RK2 was tried and also works well but is less typical in operational filters. The state propagation RK4 calculates the time derivative of the state as follows:

$$\dot{\boldsymbol{X}} = \begin{bmatrix} \boldsymbol{v} \\ \boldsymbol{a} \\ \dot{\boldsymbol{w}} \end{bmatrix} \tag{4}$$

where the accelerations are the accelerations from orbital dynamics plus the unmodeled accelerations estimated with DMC.

$$\boldsymbol{a} = -\frac{\mu}{r^3}\boldsymbol{r} + \boldsymbol{w} \tag{5}$$

The DMC estimates the unmodeled accelerations using an FOGM process [28]. The FOGM model is

$$\dot{w}(t) = -\frac{1}{\tau}w(t) + \eta(t) \tag{6}$$

with $\eta(t) \sim \mathcal{N}(0, q\delta(t-s))$. Note that the correlation time τ is the time at which the magnitude of the acceleration will fade to $1/e$ of its prior value, in the absence of additional excitation. Since the expected value of η is zero, the state propagation uses

$$\dot{\boldsymbol{w}} = -\frac{1}{\tau}\boldsymbol{w} \tag{7}$$

The state transition matrix is also propagated using an RK2 integrator, specifically Lear's formulation [29] for an RK2 propagation of the covariance with two evaluations of $\boldsymbol{A}$.

$$\boldsymbol{\Phi}(t_{i+1}, t_i) = \boldsymbol{I}_{9\times 9} + \frac{\boldsymbol{A}_i + \boldsymbol{A}_{i+1}}{2}\Delta t + \boldsymbol{A}_i\boldsymbol{A}_{i+1}\frac{\Delta t^2}{2} \tag{8}$$

where

$$\boldsymbol{A} = \begin{bmatrix} 0 & 0 & 0 & 1 & 0 & 0 & 0 & 0 & 0 \\ 0 & 0 & 0 & 0 & 1 & 0 & 0 & 0 & 0 \\ 0 & 0 & 0 & 0 & 0 & 1 & 0 & 0 & 0 \\ -\frac{\mu}{r^3}+\frac{3\mu X^2}{r^5} & \frac{3\,\mu XY}{r^5} & \frac{3\,\mu XZ}{r^5} & 0 & 0 & 0 & 1 & 0 & 0 \\ \frac{3\,\mu XY}{r^5} & -\frac{\mu}{r^3}+\frac{3\mu Y^2}{r^5} & \frac{3\,\mu YZ}{r^5} & 0 & 0 & 0 & 0 & 1 & 0 \\ \frac{3\,\mu XZ}{r^5} & \frac{3\,\mu YZ}{r^5} & -\frac{\mu}{r^3}+\frac{3\mu Z^2}{r^5} & 0 & 0 & 0 & 0 & 0 & 1 \\ 0 & 0 & 0 & 0 & 0 & 0 & -\frac{1}{\tau} & 0 & 0 \\ 0 & 0 & 0 & 0 & 0 & 0 & 0 & -\frac{1}{\tau} & 0 \\ 0 & 0 & 0 & 0 & 0 & 0 & 0 & 0 & -\frac{1}{\tau} \end{bmatrix} \tag{9}$$

For DMC the process noise covariance matrix $\boldsymbol{S}$ is added during the time update of the covariance matrix, with $\bar{\boldsymbol{P}}$ as the *a priori* covariance and $\boldsymbol{P}$ as the *a posteriori*.

$$\bar{\boldsymbol{P}}_i = \boldsymbol{\Phi}(t_i, t_{i-1})\boldsymbol{P}_{i-1}\boldsymbol{\Phi}^T(t_i, t_{i-1}) + \boldsymbol{S}_i \tag{10}$$

where $\boldsymbol{S}_i$ is calculated from the process noise covariance integral. Note that this process noise covariance integral represents the process noise spectral density $\boldsymbol{Q}$ transformed into the state space via $\boldsymbol{B}$ and then integrated from the previous measurement epoch t_{i-1} to the current epoch t_i using the state transition matrix $\boldsymbol{\Phi}$.

$$\boldsymbol{S}_i = \int_{t_i-1}^{t_i} \boldsymbol{\Phi}(t_i, \epsilon)\boldsymbol{B}(\epsilon)\boldsymbol{Q}(\epsilon)\boldsymbol{B}^T(\epsilon)\boldsymbol{\Phi}^T(t_i, \epsilon)\,\mathrm{d}\epsilon \tag{11}$$

In this paper, $\boldsymbol{S}_i$ is calculated per the formulation in NASA's Navigation Filter Best Practices [28]. Appendix B discusses the details of this implementation, showing the equations used to calculate all the γ terms for Eq. (12) and the application of this method for the backward filter (next section). Appendix B also shows how to calculate $\tilde{\boldsymbol{Q}}$ via Eq. (B12): essentially the state process noise is specified in the orbit frame and then transferred into the inertial frame for application to the inertial state. $\boldsymbol{S}_i$ is then calculated as

$$\boldsymbol{S}_i = \begin{bmatrix} \gamma_{rr}\tilde{\boldsymbol{Q}} & \gamma_{rv}\tilde{\boldsymbol{Q}} & \gamma_{rw}\tilde{\boldsymbol{Q}} \\ \gamma_{rv}\tilde{\boldsymbol{Q}} & \gamma_{vv}\tilde{\boldsymbol{Q}} & \gamma_{vw}\tilde{\boldsymbol{Q}} \\ \gamma_{rw}\tilde{\boldsymbol{Q}} & \gamma_{vw}\tilde{\boldsymbol{Q}} & \gamma_{ww}\tilde{\boldsymbol{Q}} \end{bmatrix} \tag{12}$$

C. Testing Filter on Telemetry with Simulated Debris Strike

A debris strike is applied to the spacecraft, and simulated measurements are generated per the specifications in Appendix A. Numerical values are relegated to the appendix because the focus is on methods development; specific parameters vary widely by system and thus debates about specific numbers tend to distract from the main focus of the paper. The parameters were selected to be representative of typical systems, and Appendix A includes a table indicating the wide ranges that can be expected of relevant parameters in a debris strike scenario. The default debris strike and filter parameters specified in Appendix A are used throughout this paper unless otherwise specified.

Figure 3 shows a simulated debris strike applied at $t = 7500$ s, and the results show that an abrupt change in velocity causes the filter state to diverge from the truth state for about 50 minutes. Of course,

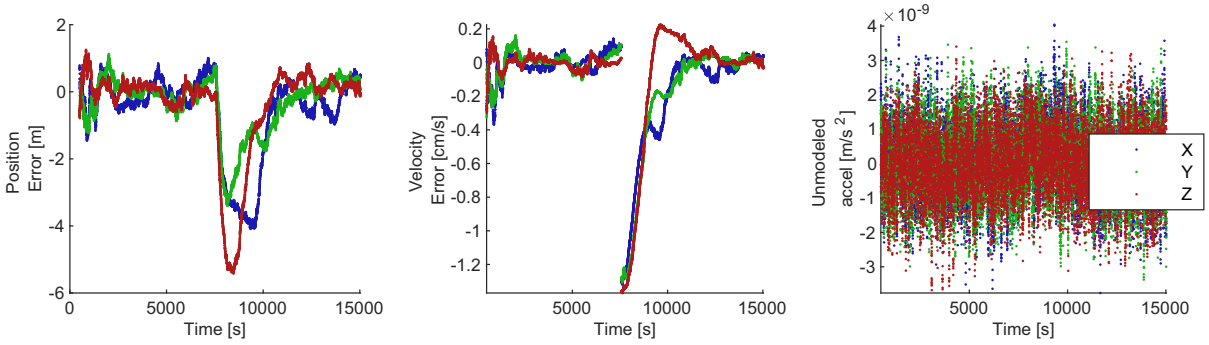

a) Position error **b) Velocity error** **c) Estimate of unmodeled acceleration**

Fig. 3 Performance of forward filter on telemetry with small debris strike.

producing this graph requires knowledge of the truth state to calculate the error in the filter's state estimate, which is not available in a real-world application. The unmodeled accelerations, which would be available in a real-world application, show a tiny feature barely distinguishable from the baseline noise.

Figure 4 shows the measurement residuals, which are typically used for assessing filter performance, indicating that this debris strike is too small to spot using the typical filter assessment method of looking for patterns in residuals.

D. Response of EKF with DMC to Debris Strike

1. *Closer Look at DMC and FOGM*

To understand the implications of this dynamic model when applied to a debris strike, some further discussion of DMC and the FOGM model is warranted. The unmodeled accelerations are initially set to zero. At each filter measurement update step, the Kalman gain maps the measurement innovation (position and velocity) into the state space (position, velocity, and unmodeled acceleration) to update the estimated state. The magnitude of this update is proportionate to the size of the measurement innovation, and is scaled by the Kalman gain. As shown in Eq. (13), the strength of the Kalman gain is effectively proportionate to the ratio of the state uncertainty (covariance) over the state uncertainty plus the measurement uncertainty (measurement noise covariance, $\boldsymbol{R}$). Therefore, a large state uncertainty and small measurement uncertainty result in measurement innovations being mapped into a large state update. *Vice versa*, a small state uncertainty and large measurement uncertainty result in a smaller Kalman gain and a smaller state update. Essentially, via the Kalman gain the filter is estimating that some unmodeled acceleration has acted on the state based on the measurement innovation it sees, and updating its estimate of the unmodeled acceleration accordingly.

$$\boldsymbol{K}_i = \boldsymbol{P}_i^- \boldsymbol{H}_i^T / (\boldsymbol{H}_i \boldsymbol{P}_i^- \boldsymbol{H}_i^T + \boldsymbol{R}_i) \tag{13}$$

With the unmodeled acceleration modeled as an FOGM process, Eq. (6) shows that the time derivative of the unmodeled acceleration, $\dot{w}(t)$, consists of two components: the first term produces a function that decays exponentially in accordance with the time constant τ. The second term $\eta(t)$ is the random noise term. The first term indicates that the unmodeled acceleration at the last timestep will also appear in the current timestep, but will have decayed slightly in accordance with the time constant τ. The measurement update calculated using the Kalman gain is added to this current estimate of the unmodeled acceleration. This allows the unmodeled acceleration to grow if measurement innovations persistently indicate that a larger unmodeled acceleration has acted on the process, and then decay away toward zero when the state has been corrected sufficiently that measurement innovations are small. Simultaneously, if the measurement innovations indicate that the state is "overcorrected," the measurement update will proactively reduce the size of the unmodeled accelerations by subtracting a state correction.

The random noise term $\eta(t)$ comes into play via the covariance matrix. In the propagation step the process noise covariance $\boldsymbol{S}_i$ is added to propagated covariance from the previous step [Eq. (10)]. This accounts for the integrated effect of process noise acting on the state from one timestep to the next, with the magnitude specified by q, the power spectral density of the acceleration noise (see Appendix B). Thus, q provides a knob to tune the strength of the Kalman gain such that the filter behaves as desired by inflating the covariance. In this case the desire is for the filter to detect when a subtle debris strike has influenced the state. Note that this deviates from typical desired filter performance, which is producing the best possible state estimate based on the most recent measurements available.

2. *Effect of Debris Strike on Filter*

In the presence of an impulsive $\Delta \boldsymbol{V}$ the truth velocity changes abruptly from the estimated state, and as the state propagates forward the position also begins to deviate. The EKF observes these measurement innovations and applies them via the Kalman gain to the *a priori* state estimate, nudging the state estimate in the direction of the truth state. At the next time step, thanks to the FOGM model, the acceleration state still incorporates that $w(t_i)$ but now at t_{i+1} it has decayed slightly in accordance with the time constant τ. This is important, because now if the state estimate has not fully corrected

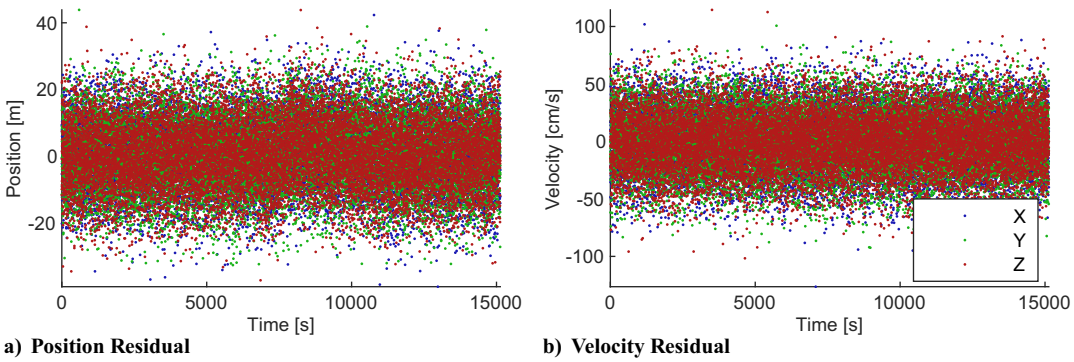

a) Position Residual **b) Velocity Residual**

Fig. 4 Measurement residuals from filter during debris strike show a minute feature that is not apparent via casual observation.

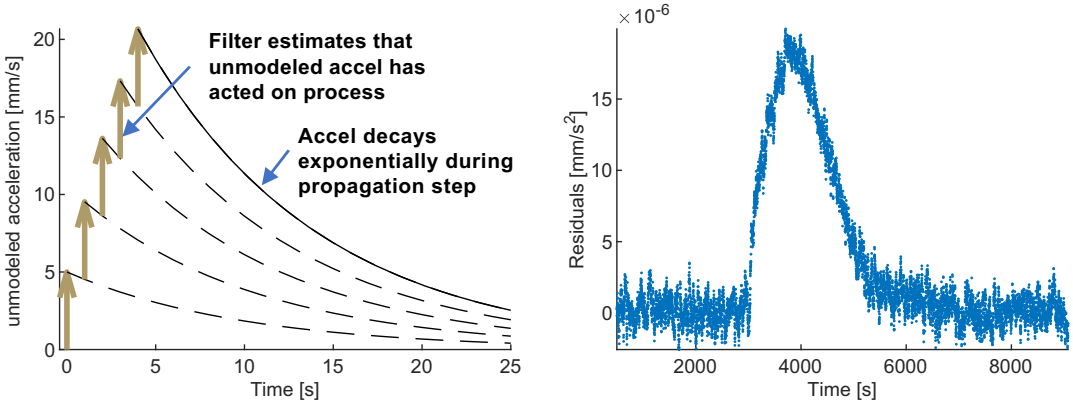

a) Stacking consecutive estimates of unmodeled acceleration **b) Filter's estimate of unmodeled accel**

Fig. 5 Illustration and example of FOGM dynamic model compensation responding to impulsive ΔV.

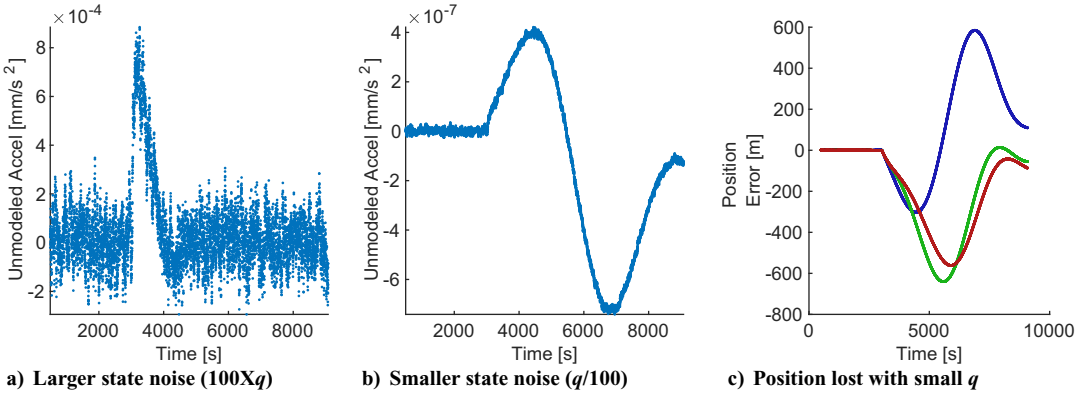

a) Larger state noise (100Xq) **b) Smaller state noise (q/100)** **c) Position lost with small q**

Fig. 6 Example of changing q to tune process noise covariance matrix. Note scales on Y axis indicating scale of unmodeled accelerations relative to Fig. 5b.

[i.e. $w(t_i)$ was not big enough to correctly capture the unmodeled acceleration], then a larger $w(t_{i+1})$ is assumed to have occurred, and is added to the acceleration state during the measurement update. This continues to happen while large measurement innovations indicate that the estimated state is not reflective of the truth state. Once innovations show that the state has converged, the unmodeled accelerations decay away, or if innovations show that it is becoming overcorrected, the measurement update will subtract an unmodeled acceleration to accelerate the decay.

Figure 5 depicts this concept, showing a conceptual diagram as well as a sample of the filter's response to an instantaneous change in ΔV. Note that this strike is 20× the magnitude of the default strike specified in Appendix A to show the pattern of the unmodeled acceleration response in the forward filter. The filter's response to the default strike is smaller and is hidden within the noise, so the pattern of the response is not clear.

Recalling that $\eta(t) \sim \mathcal{N}(0, q\delta(t-s))$, a designer might be inclined to increase q, the noise intensity, to increase the state covariance and allow the unmodeled acceleration to correct the trajectory more rapidly via a larger Kalman gain. In practice, however, a large q produces higher noise in the estimate of the unmodeled accelerations as the filter responds aggressively to noisy measurements. A smaller q improves the SNR of the feature, but a q that is too small causes the filter to lose the state estimate when the debris strike happens, as the covariance is no longer large enough to produce a sufficiently large Kalman gain able to correct the state in the presence of the perturbation. Figure 6 shows the same debris strike as Fig. 5, but with q scaled to $100 \times q$ (left) and $q/100$ (center) to illustrate the resultant filter issues. Figure 6c shows the position errors associated with the small q, indicating that the filter loses the state estimate for a prolonged period of time when q is too small (relative to Fig. 5b, where the state estimate reconverges in a reasonable amount of time). Changing τ also produces some nonintuitive behaviors. Section IV.B shows some trades to tune filter parameters to maximize strike detection for this application. Appendix A gives the baseline "initial" τ and q used to produce the results shown here, as well as the "final" τ and q after tuning.

E. Filtering Backward in Time

Most of the test statistics developed in Sec. III for identifying abrupt changes in velocity employ a state estimate obtained by running the EKF backward in time. Note that this is not the same as a backward-smoothing EKF or RTS smoother, where the fusing process incorporates all the data and thus would tend to smooth out the debris strike impulse instead of detecting it. In this application a backward-running filter that incorporates only "future" observations is required. Therefore, with the previous section's background on using an FOGM model to estimate unmodeled accelerations, the task is now to replicate this behavior when the filter moves backward in time.

The objective is to run the EKF with DMC backward through time, effectively filtering the data in the mirror image of the forward-time filter to produce a new state estimate at each data point. This backward state estimate is derived from the data that come after the data point (t_{eval}) in time and does not incorporate data that precede t_{eval} in time.[§] Thus, two state estimates can be compared at each epoch t_{eval}, one seeing only the data after t_{eval} and one seeing only the data before t_{eval}. Thus, if a debris strike occurs at t_{eval}, there is a discrepancy in the

[§]Note that the backward filter is seeded with a state estimate from the forward filter, so the backward propagation window needs to be long enough that any state corrections have been accomplished and the backward EKF's state estimate is converged, and tracking the measurement data, the influence of the initial state estimate has faded. This is analytically unsatisfying, but appears to work pretty well. The backward filter is initialized with a large covariance, which tends to de-emphasize any correlations.

velocity between the two state estimates, representative of the $\Delta \boldsymbol{V}$ that is imparted by the strike.

To accomplish this, two key aspects of the forward-filter performance need to be reproduced in backward time: the dynamic model and the unmodeled acceleration behavior. Implementing a backward dynamics model is straightforward. A negative Δt inherently causes the spacecraft to "fly backward" along its trajectory, and no changes to the basic model dynamics are required. Replicating the behavior of the unmodeled acceleration dynamics backward in time is more complicated. While an FOGM process is used to estimate the unmodeled acceleration, it is important to note that the underlying dynamics of the acceleration are not, in fact, an FOGM process. It is illustrative to examine the performance of the filter when the measurement data are reversed in time and fed into the unchanged filter. The filter's estimate of the unmodeled acceleration during the initial filtering steps is shown in Fig. 7.

Figure 7a shows that in the forward filter the estimated unmodeled acceleration decays during state propagation between timesteps. The *a priori* value at the next timestep is smaller than at the previous timestep, and then the filter adjusts that estimate up or down by applying the Kalman gain to the measurement deviation. In the reversed filter, however, the behavior is different. The state propagation causes the estimate of the unmodeled acceleration to increase exponentially during the time update, a somewhat unstable behavior resulting in large corrections that flip between negative and positive values. Note especially the scale at the top of the y axis: Just 35 data points in, the backward filter is already applying corrections to the unmodeled acceleration that are several orders of magnitude larger than the forward filter. Note that the rate of decay is set according to the time constant τ, so for the short τ's used here the effect is pronounced. A longer τ, which is more appropriate for a measurement bias or some other unmodeled dynamic effect, would have a less significant change in performance between forward and backward filters.

To explain this asymmetric behavior, recall Eq. (7) and Fig. 5. For a given timestep Δt, Eq. (7) produces Eq. (14), showing the behavior seen in Fig. 5, where the FOGM process decays exponentially as time moves forward.

$$\boldsymbol{w}(t + \Delta t) = \boldsymbol{w}(t) e^{-\Delta t/\tau} \tag{14}$$

Figure 7 shows this behavior in the forward filter, with the unmodeled accelerations decaying exponentially toward zero during the state propagation. In the backward filter, however, they are increasing exponentially, leading to excessively large accelerations applied to the filter state and requiring additional large accelerations to correct them.

To correct this, the backward filter is adjusted to employ a slightly different FOGM process: one that decays as the filter moves backward in time, in a mirror image to the forward filter behavior. This change obtains the desired FOGM behavior, shown in Fig. 8, with the accelerations decaying as the state progresses from one timestep to the other in both the forward and backward filters.

For this mirrored model, the relevant equations are as follows. Note that Δt could be either positive or negative, but this is used when Δt is negative and the filter is moving backward through the measurements. The $\boldsymbol{A}$ matrix in Eq. (9) also changes, with the sign on the $1/\tau$ now positive instead of negative in the 3×3 block on the lower right.

$$\boldsymbol{w}(t + \Delta t) = \boldsymbol{w}(t) e^{\Delta t/\tau} \tag{15}$$

$$\dot{\boldsymbol{w}}(t) = \frac{1}{\tau} \boldsymbol{w}(t) \tag{16}$$

To implement this mirrored FOGM the time constant τ is set to be negative in the backward filter. Comparing the relevant equations shows that this change essentially replaces Eq. (7) with Eq. (16) in the state propagation, and makes the necessary change to the $\boldsymbol{A}$ matrix used to propagate the state transition matrix. The remaining function where τ appears is calculating the state process noise covariance $\boldsymbol{S}_i$, and Appendix B shows that with a $-\tau$ each γ_{fwd} term is equal to the analogous γ_{bkwd} term derived using the mirrored FOGM indicated in Eq. (16). For a more general solution, the key principle is that the dynamic behavior of the processes needs to be time symmetric for the backward filter to function correctly. For the FOGM a $-\tau$ accomplishes this; for other models, alternate modifications may be needed.

One further change is required for the backward filter: similar to Fraser's [30] developments, the state process noise covariance is subtracted when filtering backward in time. This can be seen by referring to the process noise covariance integral in Eq. (11); note that $\boldsymbol{S}_i$ is derived from the integral from t_{i-1} to t_i. For the backward filter, the state process noise covariance moves from $i + 1$ to i instead of from $i - 1$ to i. Integrating backward in time results in a negative integral, but the state process noise variance needs to be added to capture the increasing uncertainty in the state estimate due to process noise from one filter step to the next. Therefore, in the backward filter $\boldsymbol{S}_i$ is subtracted. See Eq. (12) and Appendix B for implementation details. Note that this concept can alternately be applied by subtracting the state process noise covariance $\boldsymbol{Q}$, as Fraser and Potter [31] do when filtering backward.

$$\boldsymbol{S}_{i,\text{bkwd}} = -\int_{t_{i+1}}^{t_i} \boldsymbol{\Phi}(t_i, \epsilon) \boldsymbol{B}(\epsilon) \boldsymbol{Q}(\epsilon) \boldsymbol{B}^T(\epsilon) \boldsymbol{\Phi}^T(t_i, \epsilon)\, \mathrm{d}\epsilon \tag{17}$$

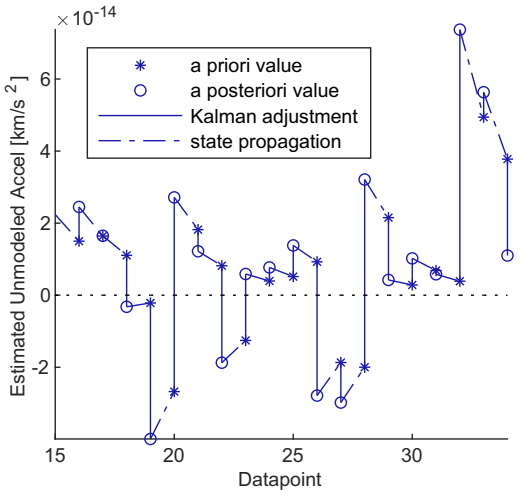

a) Forward filter initialization

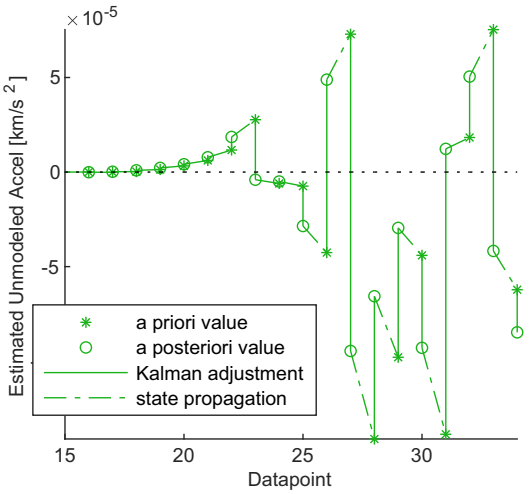

b) Backward filter initialization (no changes from forward)

Fig. 7 Comparison showing unmodeled acceleration estimation and propagation at the beginning of identical forward and backward filters. (Note: This shows the filter initialization; no debris strike is shown.)

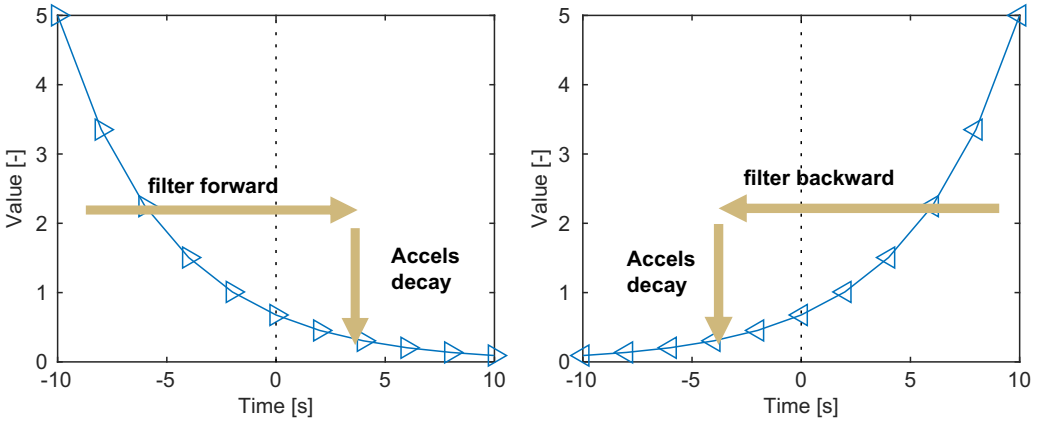

a) FOGM decaying forward in time b) FOGM decaying backward in time

Fig. 8 Traditional FOGM used in forward filtering and mirrored FOGM for backward filter.

With these adjustments, the backward filter performance, shown in Fig. 9, is comparable to the forward filter performance (Fig. 3), although it is mirrored as the filter proceeds through the data in the opposite direction.

III. Developing Test Statistics

Various test statistics are developed to accentuate the effects of a debris strike relative to the baseline noise. The intent of these test statistics is to explore various ways of postprocessing the filter state estimate to enhance the detectability of debris strike features. It is important to note that these results all show simulated telemetry, and as such the measurement noise is perfectly Gaussian and there are no additional orbit perturbations acting on the state, except in Sec. IV.D. In applying these techniques to real-world measurements all the various sources of difficult-to-characterize noise and perturbations will have a substantial effect on filter performance. It is expected that some test statistics that produce a better SNR on simulated data may perform worse on real-world data, if they require a longer period of data to function, for example. Therefore, several test statistics are investigated to produce an *a la carte* selection of techniques for on-orbit application.

A. Test Statistic 1: Difference Between Forward and Backward State Estimates

The results in Figs. 3 and 9 depend on knowledge of the truth state to produce the error in state estimate, but a proxy can be obtained by differencing the states estimated by the forward and backward filters. Figure 10 shows the difference between the forward and backward state estimates and indicates a significant feature in the velocity at the time of the debris strike. This is calculated using

$$\boldsymbol{X}_{\text{diff}} = \boldsymbol{X}_{\text{bkwd}} - \boldsymbol{X}_{\text{fwd}} \tag{18}$$

The velocity difference serves as the first test statistic evaluated for strike detection effectiveness. It also provides the estimate of ΔV,

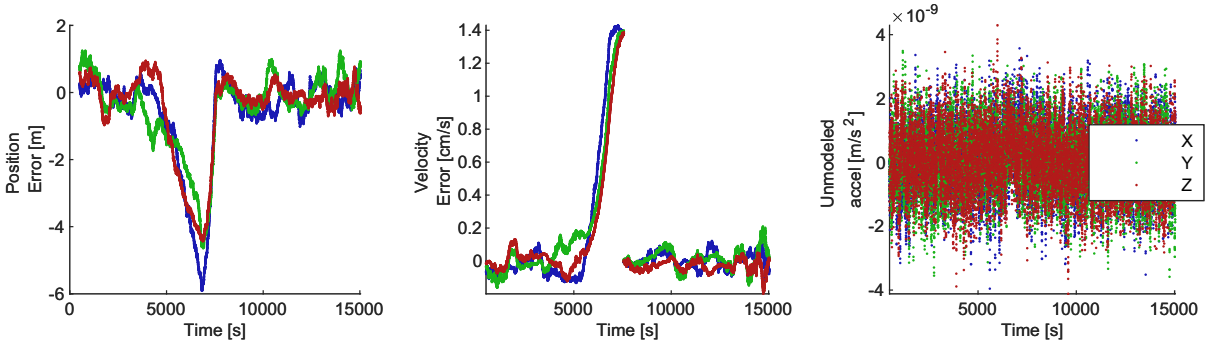

a) Position error b) Velocity error c) Estimate of unmodeled accel

Fig. 9 Performance of backward filter on telemetry with small debris strike.

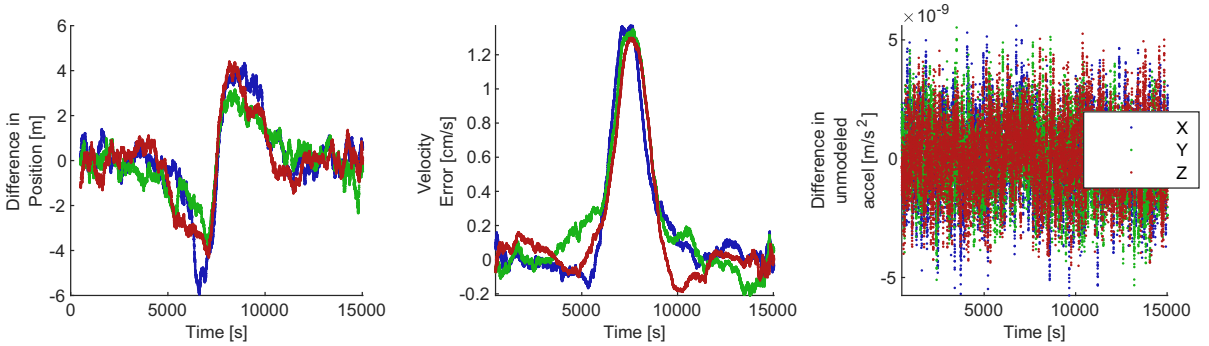

a) Difference in position estimate b) Difference in velocity estimate c) Difference in unmodeled acceleration

Fig. 10 Difference between forward and backward EKF state estimates shows significant spike in velocity without requiring knowledge of truth state.

which is used even when other test statistics are used to identify the presence of a strike.

B. Test Statistic 2: Mahalanobis Distance

The second test statistic is the Mahalanobis distance. The Mahalanobis distance expresses the generalized distance between two vectors, providing a multidimensional generalization of the distance between a point and an associated distribution. This is calculated per Eq. (19), which calculates the vector difference between forward and backward states, followed by Eq. (20), which calculates the Mahalnobis distance of that state difference relative to the expected uncertainties. Note that Eq. (19) uses the forward *a posteriori* state and the backward *a priori* state. Thus, both states are at the same epoch, but only the forward state incorporates the measurement data at that epoch.

$$\boldsymbol{X}_{M,i} = \boldsymbol{X}_{F,i} - \bar{\boldsymbol{X}}_{B,i} \tag{19}$$

$$D_{\mathrm{MH}} = \sqrt{\boldsymbol{X}_{M,i}^{T}\boldsymbol{P}_{S,i}^{-1}\boldsymbol{X}_{M,i}} \tag{20}$$

This paper investigates both full-state and velocity-only Mahalanobis distances to characterize the discrepancies between the forward and reverse filters. The full-state Mahalanobis distance is calculated using the distance between the forward and backward state estimates and the smoothed covariance [see Eq. (20), next section], while the velocity-only distance replaces $\boldsymbol{X}$ with just the velocity substate, and $\boldsymbol{P}_S$ with the corresponding central 3×3 block of the smoothed covariance. The results are illustrated in Fig. 11, which shows both full-state and velocity-only Mahalanobis distances. This overlay indicates that the baseline noise is higher in the full-state distance, so only the velocity distance is used as a test statistic as it has a higher SNR.

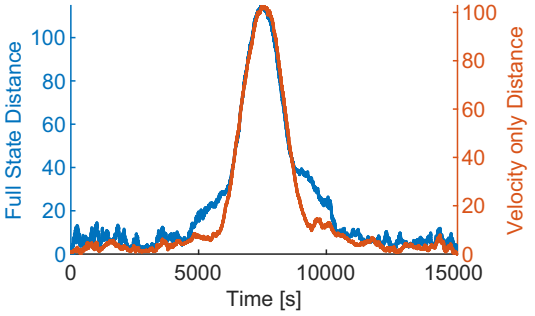

Fig. 11 Mahalanobis distances.

C. Test Statistic 3: Smoothed Accelerations from Fused Backward and Forward State Estimates

The state estimates and covariances from the forward and backward filters are fused into a smoothed estimate using a modified Fraser–Potter fixed-interval smoother [28,32]. Note that the *a posteriori* estimates from the forward filter ($\boldsymbol{X}_{F,i}, \boldsymbol{P}_{F,i}$) are fused with the *a priori* estimates from the reverse filter ($\bar{\boldsymbol{X}}_{B,i}, \bar{\boldsymbol{P}}_{B,i}$) at the same measurement time (i). Thus, like the Mahalanobis distance, all the estimates are at the same time but only the forward filter incorporates the measurement update at that time. The smoothed state estimate and covariance are calculated per

$$\boldsymbol{X}_{S,i} = \boldsymbol{W}_{F,i}\boldsymbol{X}_{F,i} + (\boldsymbol{I} - \boldsymbol{W}_{F,i})\bar{\boldsymbol{X}}_{B,i} \tag{21}$$

$$\boldsymbol{P}_{S,i} = \boldsymbol{W}_{F,i}\boldsymbol{P}_{F,i}\boldsymbol{W}_{F,i}^{T} + (\boldsymbol{I} - \boldsymbol{W}_{F,i})\bar{\boldsymbol{P}}_{B,i}(\boldsymbol{I} - \boldsymbol{W}_{F,i})^{T} \tag{22}$$

where $\boldsymbol{W}_{F,i}$ is

$$\boldsymbol{W}_{F,i} = \bar{\boldsymbol{P}}_{B,i}(\boldsymbol{P}_{F,i} + \bar{\boldsymbol{P}}_{B,i})^{-1} \tag{23}$$

The smoothed state estimates for the velocity and acceleration are shown in Fig. 12. The smoothed velocity exhibits an intuitive behavior where the smoothed estimate lies between the forward and backward filter states with the high-frequency noise removed, as shown in Fig. 12a. Note that this figure employs the truth orbit to display the errors in state estimates.

An interesting feature appears in the smoothed accelerations (Fig. 12b), which are derived from the filtering process and do not rely on knowledge of the true state. Recall that the unmodeled acceleration estimates in both the forward and backward filter are close to zero ($\sim 10^{-9}$ m/s^2) with no distinct features (reference Fig. 10). In the smoothed acceleration, however, a distinct feature appears on the order of $\sim 10^{-6}$ m/s^2. To explain this recall Eq. (23), where a weighting matrix $\boldsymbol{W}_F$ is calculated based on the ratio between the forward and backward covariances. The off-diagonal terms in this weighting matrix allow each smoothed state to be affected when a discrepancy occurs between the forward and backward states [this can be seen in Eq. (21)]. In this case, a discrepancy in the velocities is differentiated into the estimate of the unmodeled acceleration via the terms $\boldsymbol{W}_{F(7,4)}$, $\boldsymbol{W}_{F(8,5)}$, and $\boldsymbol{W}_{F(9,6)}$ (specifying the ijth term of the $\boldsymbol{W}_F$ matrix as $\boldsymbol{W}_{F(i,j)}$). This unmodeled acceleration feature is the third test statistic evaluated for debris strike detection performance.

D. Test Statistic 4: McReynold's Filter–Smoother Consistency Test

The fourth test statistic is derived from the McReynold's Filter-Smoother Consistency Test. In this test, an abrupt deviation from expected state can be identified by characterizing the consistency between the forward filter state estimate and the smoothed state

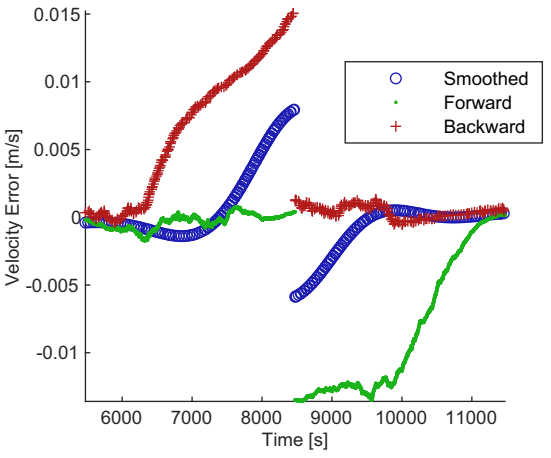

a) Smoothed velocity (X only)

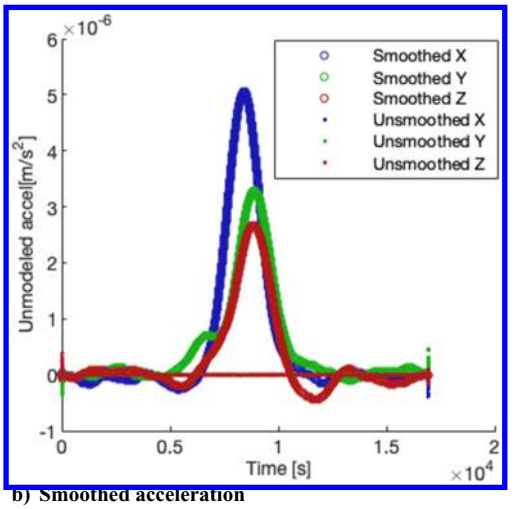

b) Smoothed acceleration

Fig. 12 Smoothed state exhibits signature in unmodeled acceleration.

estimate. First the difference between the forward state estimate and the smoothed state is found (per Wright [20]):

$$\boldsymbol{X}_D = \boldsymbol{X}_F - \boldsymbol{X}_S \tag{24}$$

$$\boldsymbol{P}_D = \boldsymbol{P}_F - \boldsymbol{P}_S \tag{25}$$

Then the McReynold's test statistic (R_m) is calculated as the ratio of each individual state ($X_{D,j}$ for state j) over the square root of the corresponding diagonal element in the covariance ($\sigma_{D,j} = \sqrt{P_{D,j,j}}$)

$$R_{m,j} = |X_{D,j}|/\sigma_{D,j} \tag{26}$$

An alternative formulation calculates a single scalar test statistic to express the consistency between the filter and smoother, rather than a separate statistic for each state. This full-state McReynold's consistency statistic is calculated via

$$R_{\text{scalar}} = \sqrt{\boldsymbol{X}_D^T \boldsymbol{P}_D \boldsymbol{X}_D} \tag{27}$$

The resultant McReynold's filter-smoother consistency statistic shows signatures in all nine states, as shown in Fig. 13. This indicates that all nine states show a feature at the time of the debris strike, but the acceleration states show the strongest feature. The scalar consistency statistic is plotted with each state on the second axis. This allows the qualitative performance of each test statistic to be observed by comparing the baseline noise on the left and right portion of the plot, away from the peak. Since the height of the peaks is matched a noisier baseline away from the peak indicates a lower SNR while a lower noise baseline indicates a higher SNR. In the position states the baseline noise is higher than it is in the scalar test statistic, while in the acceleration states it is lower, indicating that the acceleration states have a better SNR.

E. Test Statistic 5: Measurement Residuals from Propagated State Estimate

The fifth test statistic applies change detection methods to assess the measurement residuals relative to a nominal orbit propagated forward and backward from the current state estimate. The state just before the strike is propagated forward in time and the measurement residuals relative to the state estimate are determined (shown in the plots on the right side of Fig. 14). Simultaneously, the backward state estimate at $t_i = t_{\text{strike}} + 1$ is propagated backward toward $t = 0$ and compared to the measurements before the strike. Thus, both state estimates are propagated across the strike such that the state estimate does not incorporate the change in velocity, and the deviation in orbit due to the strike is observable in the measurement residuals. For reference, a simulation with no strike is also plotted in Fig. 14 to show the magnitude of the residual patterns created by the effects of the debris strike. These results indicate that the position deviations tend to be greater than the velocity deviations.

Note that the example in Fig. 14 is for a debris strike in the $-\hat{v}$ direction, which produces a change in semimajor axis and causes the residuals to build up quickly due to asynchronous periods. A debris strike in a different direction would have a less dramatic effect, but the majority of debris strikes in LEO tend to be roughly in the $-\hat{v}$ direction [33], so this provides a useful example.

Applying a change detection algorithm to this test statistic generates a scalar statistic for the entire data window surrounding a given evaluation point t_{eval}. A likelihood ratio test is employed here, which examines a specified window of data and sums the log of the likelihood ratio for each data point in that window. The likelihood ratio compares the likelihood of obtaining that data point under an assumed changed distribution over the likelihood of obtaining that data point under an unchanged distribution. Thus, if the data points as a whole tend to be more representative of a changed distribution than an unchanged distribution, the sum of the log of the likelihood ratio is

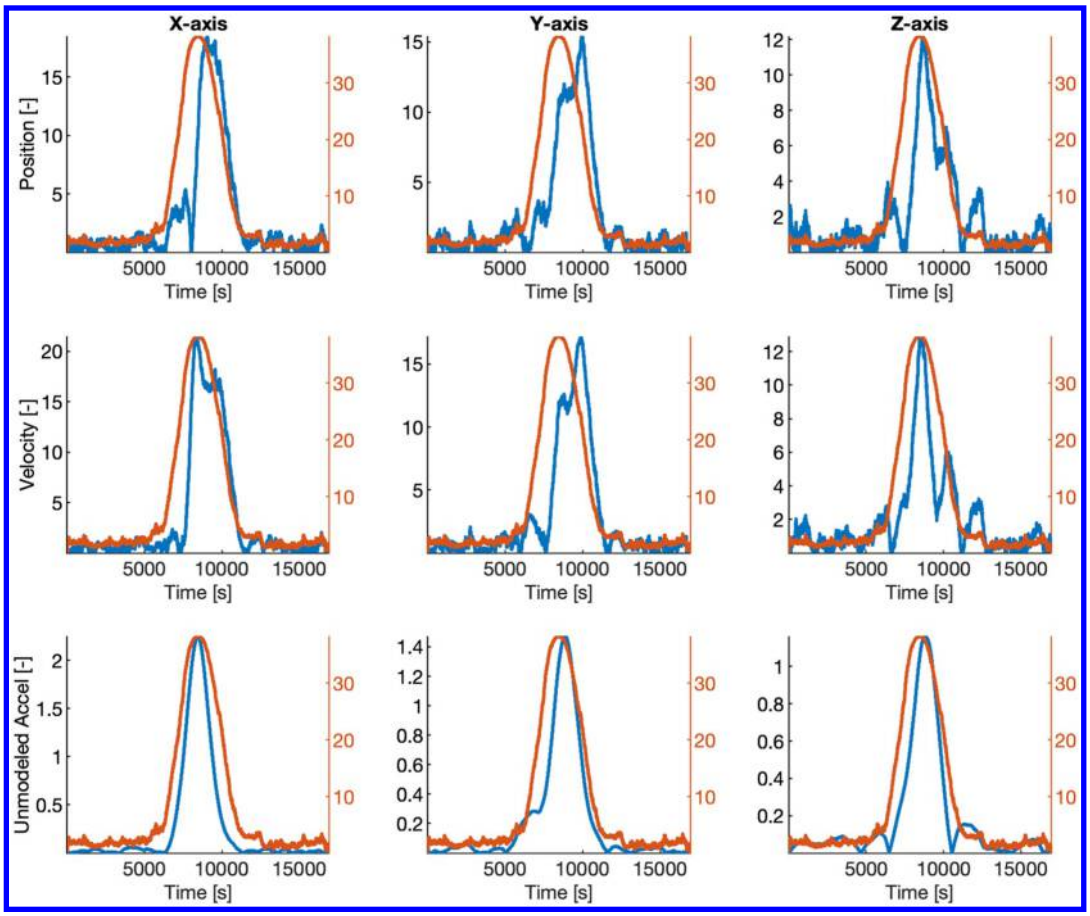

Fig. 13 McReynold's consistency statistic shows feature in all nine states. Red indicates scalar consistency statistic from Eq. (27) plotted on right axis to compare to each state from Eq. (26) (in blue, left axis).

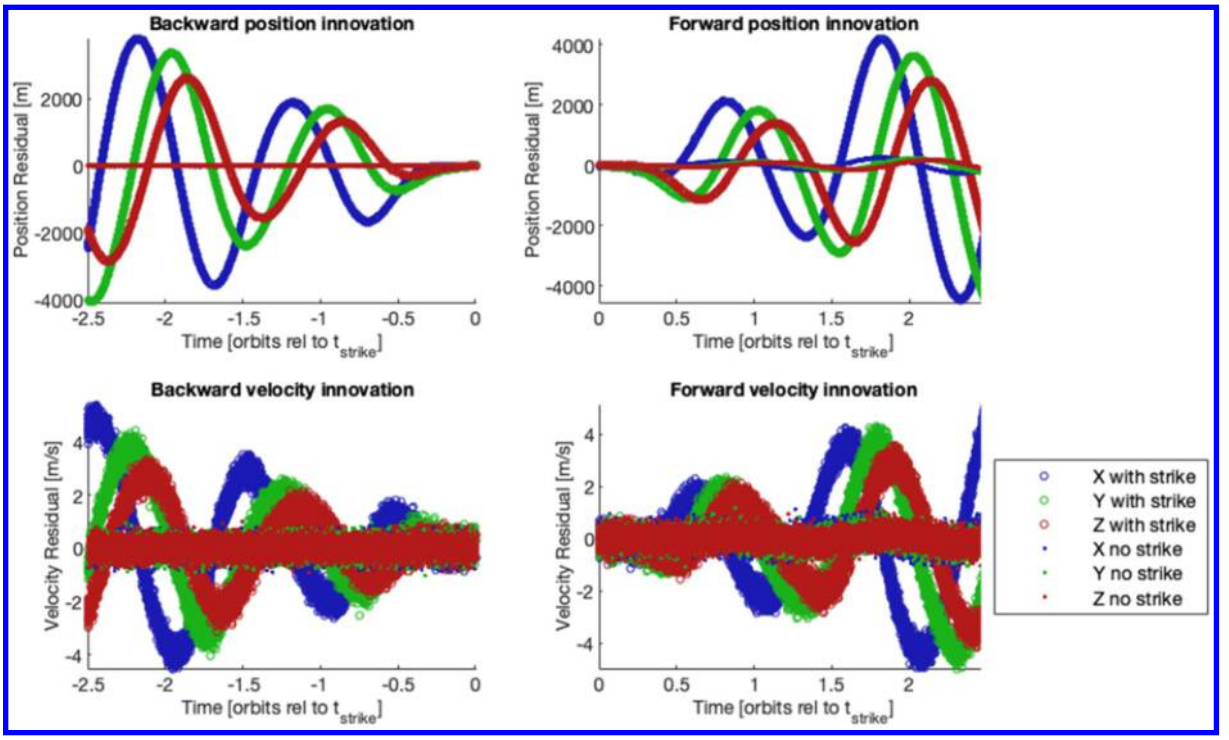

Fig. 14 Residuals generated by comparing forward and backward orbit propagation to measurements.

positive. If they are more representative of the unchanged distribution, the sum is negative.

From Moulin and Veeravalli [34] (Chap. 9), the likelihood ratio test, $\mathcal{L}$, is calculated as follows using the expected distribution of parameters when there is no debris strike $\mathcal{H}_{\text{ns}}$ and the expected distribution under a hypothesis that the distribution has changed due to a debris strike ($\mathcal{H}_s$); i.e., the patterns of propagated residuals are expected to be smaller in the absence of a debris strike, but larger in the presence of a debris strike.

$$\mathcal{L}(\boldsymbol{y}) = \frac{p(\boldsymbol{y}|\mathcal{H}_s)}{p(\boldsymbol{y}|\mathcal{H}_{ns})} \tag{28}$$

where $p(\boldsymbol{y}|\mathcal{H}_i)$ is the probability of obtaining data $\boldsymbol{y}$ given hypothesis $\mathcal{H}_i$ (i.e., the probability density function for hypothesis $\mathcal{H}_i$ evaluated at data point $\boldsymbol{y}$). The log of the resulting likelihood ratio $\mathcal{L}(\boldsymbol{y})$ is then summed across the dataset to give the test statistic T_{LLRT}.

$$T_{\text{LLRT}} = \sum \ln(\mathcal{L}(\boldsymbol{y})) \tag{29}$$

Note that this test statistic is especially sensitive to orbit perturbations that may perturb the state more slowly than a debris strike, but still significantly, and its applicability to real-world data will likely be orbit dependent. This is because a longer period of time is used to generate the test statistic. Also, this test statistic takes by far the longest to process, since the orbit must be propagated forward and backward from each point at which the test statistic is evaluated, and then the resultant noise in the distribution of those residuals needs to be characterized to develop a meaningful test statistic using a log likelihood ratio test. Since this test statistic adds substantially to processing time and is unlikely to generate results comparable to the real world, it is not included in the trade studies and comparisons of the other test statistics, but is described here. It might be well applied on systems with precision orbit determination filters/propagators or limited perturbing effects.

F. Test Statistic 6: Change in Orbital Constants

In prior work [26,35], the change in satellite mean altitude (dSMA) is used to identify orbit perturbations. For comparison to these efforts, the change in semimajor axis is used for the sixth test statistic. However, a dSMA will only occur if a strike changes the magnitude of the spacecraft velocity. Out-of-plane ΔV components will change the orbit plane, but not the semimajor axis. ΔV components that change the direction of the velocity but not the magnitude will likewise not change the semimajor axis. Therefore, for this test statistic three orbital constants are used: the traditional dSMA, the eccentricity e, and the direction of the orbital angular momentum (h_{dir}). It is worth noting that in many LEO orbits the prevalent debris flux is near head-on [33], so the dSMA alone would likely be a strong indicator for many collisions, but for other orbits, like GEO, prevalent fluxes may occur in other directions, so the more general solution using three orbital constants is developed here. See discussion for additional cautions on using an orbit change detector with highly directional sensitivity.

The orbital constants are calculated using only the forward-filter state, to represent a straightforward application requiring minimal postprocessing of existing data. Using the filter's estimate of the position $\boldsymbol{r}$ and velocity $\boldsymbol{v}$, the semimajor axis a, eccentricity e, and orbital angular momentum $\boldsymbol{h}$ are calculated as follows. The magnitudes of the position and velocity are denoted r and v, respectively, while μ represents the geocentric gravitational constant.

$$a = \frac{1}{(2/r) - (v^2/\mu)} \tag{30}$$

$$\boldsymbol{e} = \frac{[v^2 - (\mu/r)]\boldsymbol{r} - (\boldsymbol{r}\cdot\boldsymbol{v})\boldsymbol{v}}{\mu} \tag{31}$$

$$\boldsymbol{h} = \boldsymbol{r}\times\boldsymbol{v} \tag{32}$$

To reduce the direction of the angular momentum to a scalar test statistic, the azimuth and elevation of the angular momentum unit vector are calculated (i.e., in spherical coordinates as expressed in the inertial frame), and then the root-sum-square of these values is taken to obtain a scalar representing the current direction of the orbital plane. Note that this is an approximation that assumes small angles, but since the intention is just to reduce the change in orbit plane to a scalar this is adequate for this application.

With these scalar test statistics, changes in the orbital state due to impacts in any direction in the orbit frame are rendered observable.

A strike in the velocity direction produces changes in the semimajor axis and eccentricity, a strike in the radial direction produces a change in eccentricity, and an out-of-plane strike produces a change in the direction of the orbit plane. In previous test statistic examples, the strike is applied evenly on the inertial X, Y, and Z axes, but in this example the strike is applied evenly across the three directions of the orbit frame to produce a change in each of these test statistics.

Since these test statistics can be applied without reversed filters or smoothing, the filter parameters are adjusted to be more typical of standard operations. In Fig. 15, the process noise q is inflated to be more representative of a typical navigation filter. The value used is 100× the initial default value for q shown in Appendix A. In the prior test statistics the filter is designed to allow the state to deviate to make the debris strike more observable, but the intention of this test statistic is to compare to "typical" methods so that the filter is retuned toward a more traditional performance, where the covariance is tuned to correct the state quickly in the presence of perturbations to maintain an accurate state estimate based on the available data.

IV. Tuning, Comparison, and Performance Assessment

To evaluate the filter's performance a streaming implementation is introduced to analyze a data series and identify strikes without *a priori* knowledge of the strike time. The forward filter is applied once across the entire dataset (in online analysis this could be updated persistently as telemetry is received). Then the test statistics are calculated using a sliding window where all test statistics are evaluated at t_{eval}, which is situated a fixed interval behind the leading data point in the window. Thus, the backward filter can be applied backward through the data and across t_{eval}, and then the smoother, allowing the calculation of each test statistic at t_{eval} based on data windows surrounding t_{eval}. Since the test statistics show a spike in the presence of a debris strike, an "integrated" test statistic is stored as well as the peak value, to determine if that improves the detectability of the debris strike feature.

A. Normalizing Test Statistics as SNR

Each test statistic is calculated at each t_{eval}. The peak value of each test statistic is stored and also a window of data is empirically integrated to form an integrated test statistic, to see if that produces a stronger signal. To compare test statistics against each other, each value must be normalized. This is done by calculating the SNR of each test statistic, where the baseline noise is calculated in a long simulation with no debris strike applied.

Calculating the detectability threshold T_{thres} from the baseline noise is a nontrivial exercise on simulated data and is even more complicated on real data. The core of the challenge lies in assessing the desired probability of false alarm versus probability of missed detection. A higher detection threshold will result in fewer false alarms but may miss some detectable strikes, while a lower threshold will detect more strikes but also return a high rate of false alarms. Figure 16 shows a diagram of this decision, which is inherently application dependent: for some applications a low false alarm rate may be paramount, while for others a high chance of detecting small strikes may be preferred. The blue curve shows the probability density function (pdf) of the test statistic output when no debris strike is present. The red shows the pdf when a given debris strike has occurred. Depending on where the threshold is set (dashed black line), the probability of false alarm can be smaller or larger, and the probability of missed detection will become larger or smaller according to the same threshold.

For this paper, the thresholds are determined by setting a desired rate of false alarm of one per week. With this rate of false alarm and a given telemetry rate a target probability of false alarm is established. A long simulation is conducted to establish the baseline noise inherent in each test statistic when no debris strike is present. An example is shown in Fig. 16a, with the test statistic output evaluated at 200,000 data points and the resultant baseline noise, with no debris strike, plotted. The characteristics of the distribution of this noise varies depending on test statistic, so a kernel distribution is fitted to the noise, as shown in Fig. 16c.

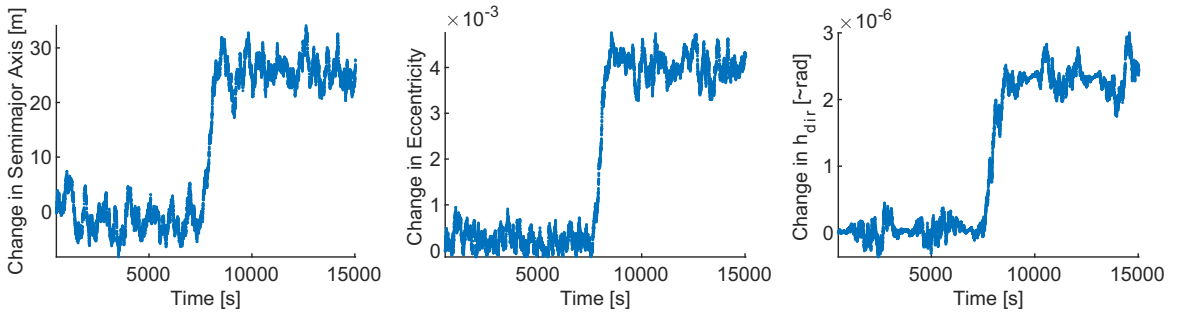

a) Change in semimajor axis b) Change in eccentricity c) Change in angular momentum direction

Fig. 15 Orbital constants calculated from forward-filter state estimates show change at time of strike.

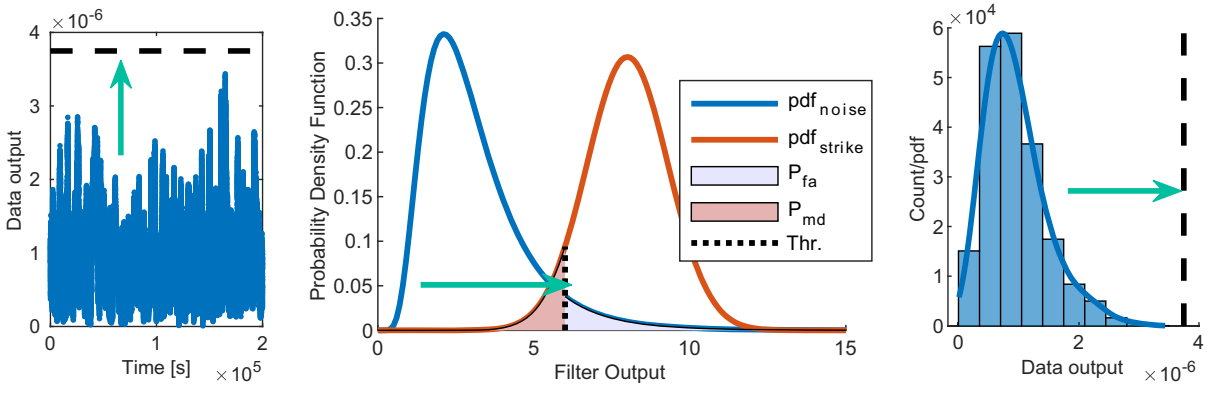

a) Data with threshold b) Concept for setting thresholds c) Histogram and pdf

Fig. 16 Depiction of process for setting detection thresholds. Left: Goal is to set threshold above baseline noise, which varies. Center: Probability density functions of filter output with and without debris strike. Right: Kernel distribution fitted to histogram of filter output with no debris strike used to establish threshold.

From this distribution and the desired probability of false alarm the detection threshold T_{thres} is set; i.e., it is set at a point where the remainder of the tail of the distribution, above the threshold, corresponds to the desired false alarm rate. With this detection threshold the SNR of a given test statistic in the presence of a given debris strike is calculated. A debris strike is applied repeatedly to the simulation in a Monte Carlo, with randomized strike time and orbit location, to establish the magnitude of each test statistic's response to the debris strike by averaging the response across all Monte Carlo runs. The magnitude of this response divided by the detection threshold is saved as the SNR for the test statistic. Thus, the various test statistics can be compared to each other to assess their relative performance in detecting strikes.

B. Tuning τ and q

Typically q is tuned to obtain a covariance that bears the desired scale relative to the state errors (i.e., an appropriate number of data points fall within the 3σ boundary) or to minimize state errors. In this application, however, the goal is not to obtain the best possible state estimate at each time, instead the goal is to detect debris strikes. A traditionally tuned filter might tend to correct the state too quickly and smooth out the debris strike, whereas in this case it is desired to let the effects of the debris strike affect the state for long enough to cause a detectable signal. Note that τ is also a tuning parameter, and while intuitively a short τ might mimic a short debris pulse, in practice it can fail to accumulate a substantial enough acceleration quickly due to the mechanics depicted in Fig. 5a. These two influences interact and a trade study is required to determine which combination of τ and q produces the best SNR.

An initial trade study is conducted to understand the relationships between τ, q, and the SNR for the various test statistics. A subset of results is shown in Fig. 17. These indicate that there is a clear zone where τ and q produce a higher SNR, but that this zone varies somewhat between the test statistics. In general, a smaller q and larger τ produce an equivalent or sometimes improved test statistic, but with a smaller q the filter tends to diverge from the truth state for longer when an unexpected acceleration occurs, so the larger q and smaller τ are selected. The red star in the figure is at $\tau = 1$ s and $q = 2.15\text{e} - 17\ \text{m}^2/\text{s}^5$, which produces a strong SNR in most test statistics. Note that the acceleration test statistics produce a noticeably higher SNR than the velocity-related test statistics.

Figure 18 shows these trade studies superimposed for a single τ, to illustrate the relationship between q and SNR for each of the test

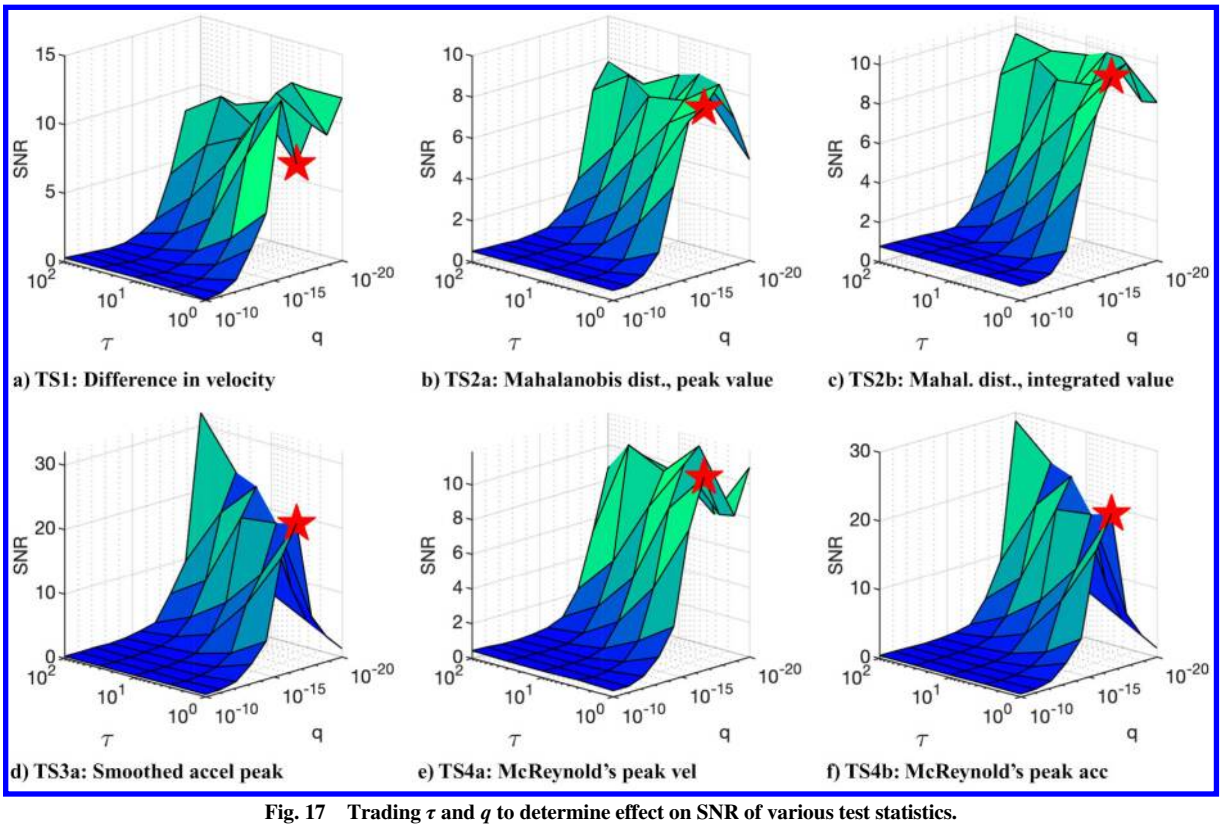

Fig. 17 Trading τ and q to determine effect on SNR of various test statistics.

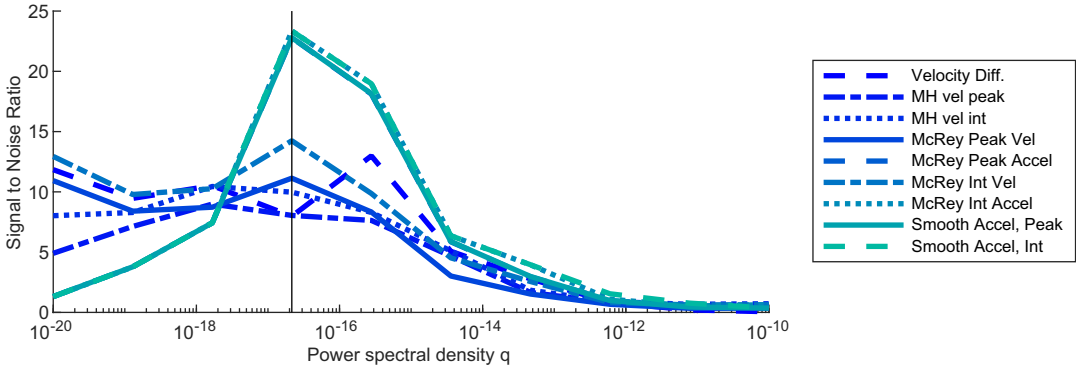

Fig. 18 Superimposing SNR from various test statistics to compare results for given time constant τ.

statistics. This shows that the best test statistics are the smoothed accelerations and the McReynold's consistency statistic for accelerations, but it is important to remember that some other test statistics may perform better in the real-world where additional orbit perturbations may affect the state. Orbit perturbations typically affect the state more slowly than a debris strike, so test statistics that require a long span of data may perform well on simulated telemetry but struggle in real-world applications.

C. Performance when Detecting and Estimating Unknown Strikes

A Monte Carlo is conducted that randomizes the strike magnitude and direction and orbit parameters (inclination and true anomaly) such that the strike is applied randomly relative to the orbit frame of the satellite. For each strike each test statistic is calculated, and the test statistics that detect the strike are recorded along with the estimated size of the strike, if it is detected, as shown in Fig. 19. Note that false alarms are not characterized in this analysis, but missed detections are shown along the x axis. The colors of the plot indicate the number of test statistics that successfully identified the strike on each axis, noting that the "RSS" axis also includes the scalar test statistics: Mahalanobis distance and change in orbital constants. This Monte Carlo uses the τ and q identified in the trade study in the prior section.

While the detectability of some strikes seems improbably small, similar real-world capabilities have been demonstrated by Exoanalytic Solutions, which identified an unexpected in-track ΔV of approximately 0.7 mm/s shown in Fig. 2 [14]. Also, characterizing the noise baseline using a kernel distribution provides a decent proxy for the detectability threshold, but with a fairly short data set to develop the no-strike noise distribution false alarms may still occur. Conducting trade studies with long datasets requires excessively long computation times without adding much to this content, so shorter runs are used since the intention of this paper is to explore the problem using simulated data. Specific noise levels will change, likely dramatically, with each individual on-orbit system.

D. Performance in the Presence of Orbit Perturbations

The primary challenge of applying these techniques to real-world systems will likely be separating debris strike perturbations from other orbital perturbations and telemetry idiosyncrasies. In prior work, algorithms have been applied to detect rotational momentum changes in the attitude telemetry of NASA spacecraft and found abundant unexpected features that complicate detection of debris strikes [19].

While modeling the unknown is always a challenge, a quick proxy assessment is performed by adding J3 perturbations and drag perturbations to the simulated truth state, but not to the filter dynamics. To accentuate the effects of these perturbations the orbit is lowered to 400 km (from the default 800 km) and the eccentricity rose from 0 to .001 (the lower orbit is necessary to show the effects of drag on the short time scales seen here). To produce a signature higher than the noise in the presence of these perturbations, the debris strike magnitude is increased by 2×.

The acceleration due to drag is added to the orbit state per Chapter 8 of Vallado and McClain [36]. The parameters used to calculate drag are specified in Appendix A. Note that the solar array is rotated relative to the velocity throughout the orbit, as if it were tracking the sun, which causes the drag applied to the spacecraft to vary as it would on orbit, with ϕ and θ determined such that the array always points in the inertial X direction regardless of the satellite location. However, the density of the atmosphere only varies with altitude, without seeing the variability throughout the orbit that would be experienced in reality. All vectors here are expressed in the inertial frame.

$$\boldsymbol{a}_{\text{drag}} = -\frac{1}{2}\frac{C_D A_{\text{tot}}}{m_s}\rho v_{\text{rel}}^2 \frac{\boldsymbol{v}_{\text{rel}}}{v_{\text{rel}}} \tag{33}$$

$$A_{\text{tot}} = A_{\text{bus}} + A_{\text{array}}\cos(\phi)\cos(\theta) \tag{34}$$

$$\rho = \rho_o e^{-(r-r_o)/H} \tag{35}$$

The following acceleration due to J3 perturbations is added to the orbit state, per Eq. (11.65) in Schaub and Junkins [37].

$$\boldsymbol{a}_{J_3} = \frac{1}{2}J_3\frac{\mu}{r^2}\left(\frac{r_{\text{eq}}}{r}\right)^3\begin{pmatrix} 5\left(7\left(\frac{Z}{r}\right)^3 - 3\left(\frac{Z}{r}\right)\right)\frac{X}{r} \\ 5\left(7\left(\frac{Z}{r}\right)^3 - 3\left(\frac{Z}{r}\right)\right)\frac{Y}{r} \\ 3\left(1\text{–}10\left(\frac{Z}{r}\right)^2 + \frac{35}{3}\left(\frac{Z}{r}\right)^4\right)\end{pmatrix} \tag{36}$$

While J2 is neglected, it is also straightforward to capture J2 in Kalman filter dynamics. Capturing an estimate of J3 and drag is only a little less straightforward, so this represents the efforts of a rather mediocre filter, and shows that a small strike is still detectable even in the presence of unrealistically severe unmodeled orbit perturbations.

The results in Fig. 20 show that adding these unmodeled dynamics causes additional noise in the test statistics, as expected. The filter's estimate of the unmodeled acceleration successfully estimates these unmodeled perturbations so that the filter stays converged, but this produces additional noise in the filter output and increases the noise floor of the filter, obfuscating the effect of the debris strike. However, a somewhat larger strike is still detectable, which is still well into the size regime of hazardous nontrackable debris. Refer to Appendix A for specific debris sizes and impact parameters. It is worth noting that these J3 and drag perturbations are currently completely unmodeled in filter dynamics, but these and more are accounted for in precision orbit determination filters, so the performance of real-world systems could be better than what is shown here.

Figure 21 repeats the trade from Fig. 18, but with the perturbations added to the state and the orbit lowered to 550 km and debris strike size increased by 5×. Comparing to the previous trade, it can be seen that the best performance occurs with a somewhat larger q, as a larger q allows the filter to track the perturbed state more accurately. With a well-converged filter state the larger debris strike still causes a detectable signal in the presence of noise due to J3 and drag.

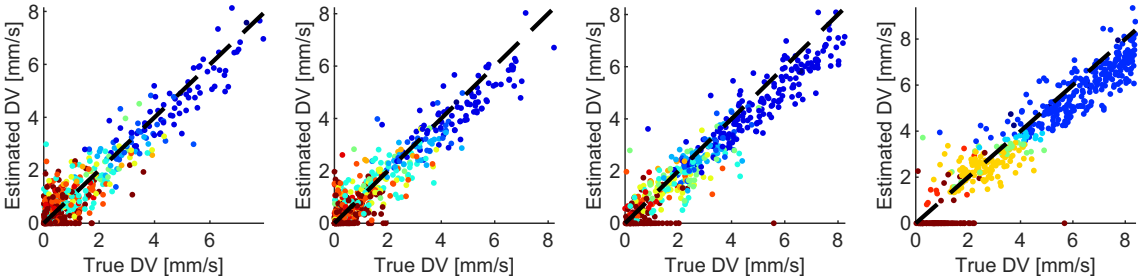

a) Strike size estimate in X-axis **b) Strike size estimate in Y-axis** **c) Strike size estimate in Z-axis** **d) RSS magnitude**

Fig. 19 Monte Carlo analysis indicating estimated size of random strike relative to true strike. Color indicates number of test statistics that detected each strike.

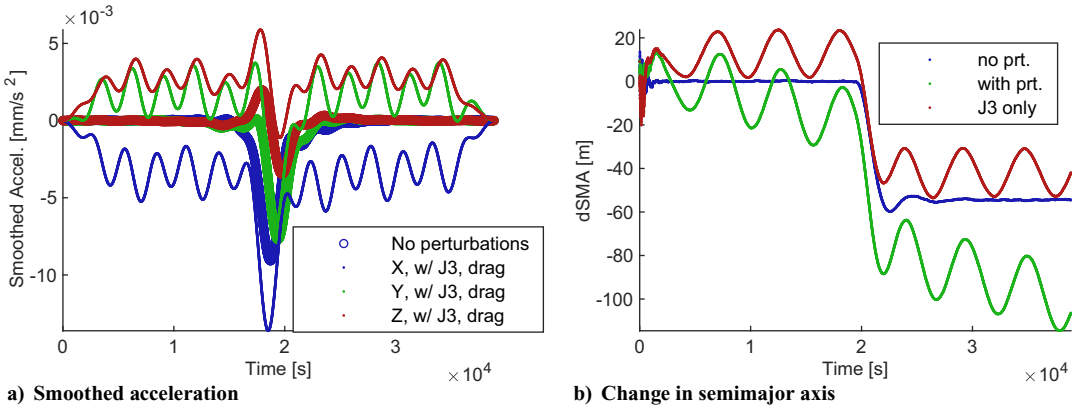

a) Smoothed acceleration b) Change in semimajor axis

Fig. 20 Simple perturbation models (J3 and drag) added to truth state but not filter dynamics show that baseline filter noise is higher, but strikes are still detectable. This plot shows a 400 km orbit and a debris strike that is 2X the magnitude of the default strike (see Appendix A).

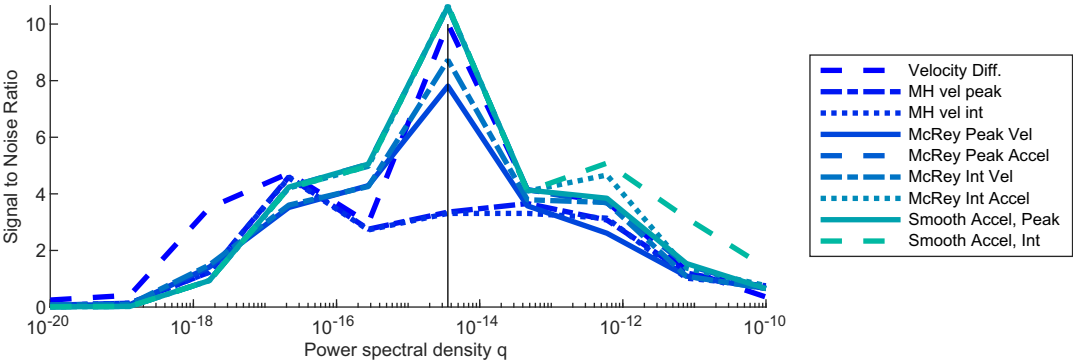

Fig. 21 Superimposing SNR from various test statistics to compare results for given time constant τ. Note that preferred q is now larger than the trade without perturbations, and the SNR is smaller even with a larger strike.

E. Final Comparison Between Measurement Residuals and Test Statistic Output

As a final observation, Fig. 22 shows the pattern of measurement residuals from the forward EKF with no test statistics or postprocessing. Patterns of filter residuals are typically used to assess filter performance and screen for unexpected features. These residuals indicate that standard practices for observing filter performance are much less sensitive to debris strike features than the test statistics developed herein. The output from the smoothed acceleration test statistic is compared to the measurement residuals for two debris strikes: the small one is 1/10th the default strike specified in Appendix A, and the large one is 2X the default strike specified in Appendix A. This shows that a large strike begins to show up in the measurement residuals of a typical filter, but the test statistic produces a much stronger signal for detecting subtle strikes.

V. Discussion

The magnitude of detectable strikes is highly dependent on system parameters. These numbers are only placeholders and do not prove a capability; real system data must be used to determine detectable ΔV thresholds. Therefore, while these metrics are promising in terms of being able to detect minor impacts from hazardous nontrackable debris, the quality and usefulness of data obtained will likely be system dependent, and not all systems may have the precision orbit determination required to separate abrupt unexpected changes produced by debris strikes from routine changes due to gravity effects, drag fluctuations, etc.

While implementing these methods in the presence of real-world orbit perturbations will be a challenge, precision orbit determination tools exist and can be leveraged when implementing these methods on active spacecraft. It is more efficient to develop methods using basic models and then apply these methods to real data and characterize the results rather than exhaustively modeling perturbations, even though they are critical to detection thresholds. Sensor noise characteristics present a similar complication; sensor noise and irregularities can be very challenging to model accurately but are a critical element for accurately predicting detectability thresholds. The exact magnitude of detectable orbit changes may vary, but on-orbit experience has proven that the capability is possible. Several spacecraft [9,35] have detected orbit changes in conjunction with minor anomalous events and thereby detected debris strikes, so it seems likely that improving these orbit change detection capabilities, as illustrated in this paper, will result in an improved ability to detect minor debris impacts in the typical course of operations.

This paper leverages simulated GPS telemetry, but these methods could conceivably be applied to non-cooperative and uncontrolled objects to obtain a larger population of *in situ* measurements. The detection thresholds would likely suffer, but with LeoLabs and other companies providing increasingly precise orbit determination services, it is possible that the increasing precision required for space traffic management in the emerging space era will allow methods like this to be applied broadly to populations of objects on orbit. For example, ExoAnalytic Solutions has already demonstrated an impressive capability to detect similar events on GEO satellites, and maintains routine observations of objects in GEO [14]. Combining capabilities and datasets from various providers could likely generate a rich dataset for validating and tuning debris environment models.

This is critical in the emerging space era as burgeoning populations of satellites are operated by commercial entities and emerging state actors. Most established players follow more stringent debris guidelines than are required by international systems, but for newer space operators it is important to incentivize compliance with space sustainability initiatives. Previous work [35] has indicated a mismatch between debris risks assessed using heritage methods and events experienced on orbit, which is not a sustainable *modus operandi* to motivate appropriate behavior from new space actors. Model predictions must be consistent with operator experience; otherwise

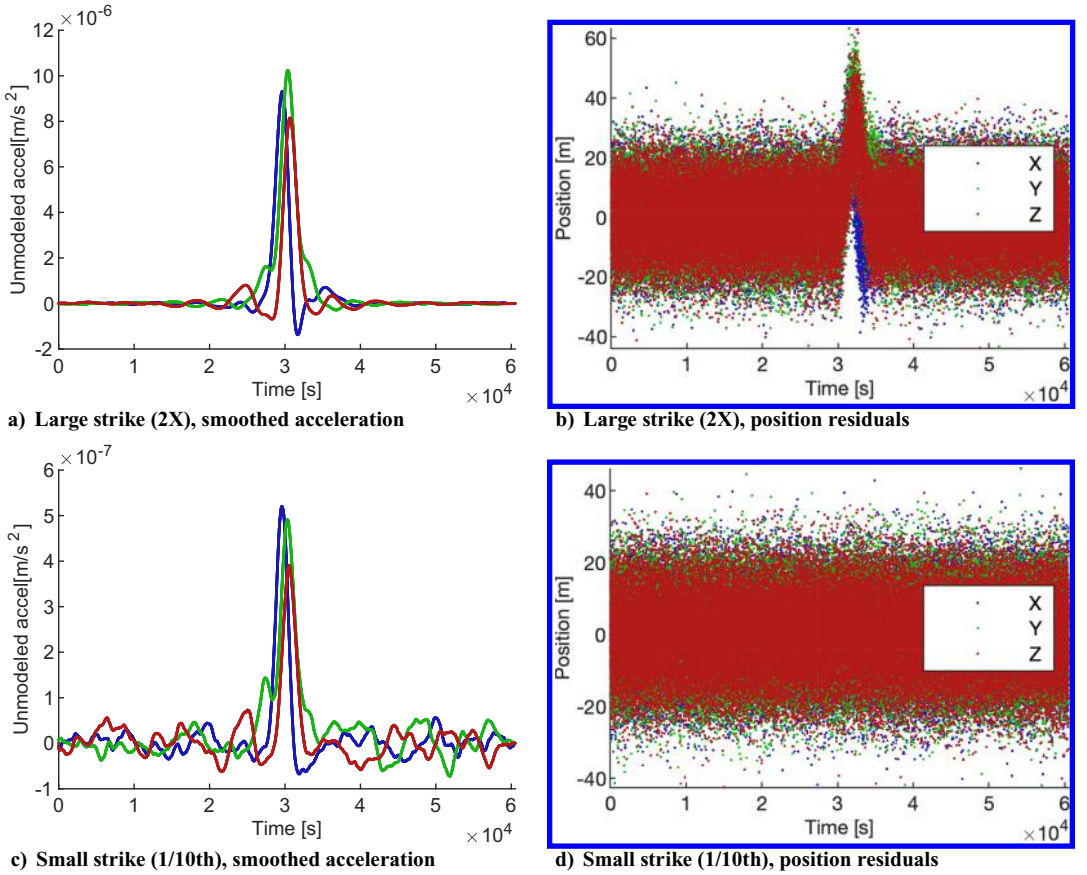

a) Large strike (2X), smoothed acceleration

b) Large strike (2X), position residuals

c) Small strike (1/10th), smoothed acceleration

d) Small strike (1/10th), position residuals

Fig. 22 Comparing test statistic output to traditional measurement residuals in the presence of large and small debris strikes. Test statistic shows strong signal in response to strike far too small to see in measurement residuals.

operators may leverage a loose legislative environment and disregard safe practices to the detriment of the long-term debris environment. This paper investigates a method to use on-orbit data to detect debris strikes so that operators can be cognizant of their local debris environment and to potentially provide additional data to tune orbital debris environmental models and methods and inform decisions on legislation and debris mitigation requirements and remediation investments.

The heritage method of detecting debris strikes via a change in satellite mean altitude produces a strong test statistic, but it is primarily sensitive to debris strikes in the $\hat{\boldsymbol{v}}$ direction. With current LEO populations this may be justified, as models predict that most debris strikes will occur near this direction. However, it has limitations as radial or out-of-plane components of strikes are not observable. Breakups occurring in GTO or Molniya orbits are already difficult to characterize, so using a debris strike detection system that can only detect the expected debris strikes introduces a strong confirmation bias within the measurement system, which should make any scientist cringe. To maintain a clearer picture of the debris environment it is important to have direction-agnostic and orbit-agnostic debris-sensing systems, like the techniques developed in this paper.

As the emerging space era puts thousands of new satellites on orbit at an accelerating rate, it is especially critical to characterize the hazardous nontrackable debris environment. Accurate, timely information is crucial to shaping policy, legislation, mitigation, and remediation initiatives, and these initiatives are essential to ensuring a sustainable future for the global space enterprise.

VI. Conclusions

An EKF with DMC can be adapted to accentuate abrupt orbit changes that are too small to show a feature in the pattern of filter residuals typically used for filter performance assessment. Various test statistics derived from the filter output provide strong signals to allow detection of subtle changes indicative of minor debris strikes. The strongest of these test statistics are derived from the smoothed unmodeled acceleration, obtained when the smoother fuses estimates from separate forward and backward filters. This is similar to the Fraser–Potter smoother, and a necessary adaptation is ensuring that the backward filter employs a mirrored model for the unmodeled acceleration behavior such that filter performance is symmetric when filtered forward and backward in time. These methods offer a capability for spacecraft operators to monitor the state of health of their spacecraft and, with a sufficient population of data, could provide *in situ* data for tuning debris environmental models and risk assessment processes.

Appendix A: Default Values for Parameters

This appendix specifies values that are used for parameters unless they are otherwise specified in the text. Debris strike parameters are inherently probabilistic and vary by orbit, so specifying a value often sparks debate that distracts from more relevant debates about methods. Therefore, an entire table of values is provided here in Table A1 to specify debris strike and spacecraft parameters that could produce the baseline ΔV and the scaled ΔV's used in various simulations throughout this paper. The table is shaded in accordance with the likely hazard presented by the piece of debris and its detectability. As shown, the hazardous nontrackable debris pieces (orange) represent a large percentage of the strikes that are applied in this paper. Some systems could push the detectability threshold low enough that even nondamaging strikes could be detected (blue), and some systems (large spacecraft and/or spacecraft with substantial unmodeled perturbations) could have detection thresholds corresponding to debris that is potentially trackable. However, steel debris, typically modeled as spheres, currently drives the risk to LEO spacecraft, and this table indicates that detection thresholds are likely in the range where this type of debris could be detected to acquire more information about the hazardous nontrackable debris population.

Table A1 Table illustrating myriad situations that could produce a detectable ΔV for a hazardous nontrackable piece of debris

				Densities, in g/cm^n:			2.7	8.05	0.04269	1.8	8.96
Regime	Scale	Mass S/C (kg)	Mass db (g)	Velocity (km/s)	MEF	DV (cm/s)	Aluminum sphere diameter (cm)	Steel sphere diameter (cm)	Square of MLI (cm, on edge)	1-mm-thick square CFRP (cm)	Length of 2-mm-diam copper wire (cm)
LEO	Default	200	0.2	12	2	2.4	0.52	0.36	2.16	1.05	0.71
LEO		100	0.1	12	2	2.4	0.41	0.29	1.53	0.75	0.36
LEO		10	0.01	12	2	2.4	0.19	0.13	0.48	0.24	0.04
LEO		1000	1	12	2	2.4	0.89	0.62	4.84	2.36	3.55
LEO	2X	200	0.4	12	2	4.8	0.66	0.46	3.06	1.49	1.42
LEO		100	0.2	12	2	4.8	0.52	0.36	2.16	1.05	0.71
LEO	5X	200	1	12	2	12	0.89	0.62	4.84	2.36	3.55
LEO		100	0.5	12	2	12	0.71	0.49	3.42	1.67	1.78
LEO	1/10th	200	0.02	12	2	0.24	0.24	0.17	0.68	0.33	0.07
LEO		1000	0.1	12	2	0.24	0.41	0.29	1.53	0.75	0.36
GEO	Default	200	6.857143	0.7	1	2.4	1.69	1.18	12.67	6.17	24.36
GEO		2000	68.57143	0.7	1	2.4	3.65	2.53	40.08	19.52	243.60

Key:	Likely too small to cause damage	Hazardous nontrackable	Potentially trackable

Scale refers to debris strike magnitude as specified throughout the paper. Debris listed as "potentially trackable" is *not* tracked currently, but may be tracked as current state-of-the-art systems mature.

Density units are g/cm^3 for aluminum, steel, and copper, g/cm^2 for MLI and CFRP. Abbreviations used in table: S/C = spacecraft, Mass db = mass of the debris, MEF = momentum enhancement factor, DV = change in velocity, MLI = multilayer insulation, CFRP = carbon fiber reinforced plastic.

The intention of moving values to the appendix is to ensure that the focus of the paper stays on methods development, the actual parameters will vary widely by system, and the detectability of small debris strikes will vary widely as well. Ultimately, spacecraft have detected strikes with no specialized filtering, so introducing a filter that can accentuate the subtle effects of strikes can only improve their performance as detectors and result in a larger body of data for assessing the debris environment. The parameter values used throughout this paper are provided in Table A2, and any deviations from these values (i.e., for trade studies, etc.) are specified in the text.

Appendix B: Derivation of Process Noise Covariance for Mirrored FOGM in Backward Filter

In the backward filter, the traditional FOGM, which decays exponentially as time advances, results in estimates of the unmodeled

Table A2 Default parameters used in simulations throughout unless otherwise specified

Parameter	Value	Unit
Spacecraft parameter		
S/C mass	200	kg
Orbit parameters		
Orbit altitude	800	km
Orbit eccentricity	0	— —
Orbit inclination	40	deg
Orbit right ascension of the ascending node	30	deg
Orbit argument of perigee	50	deg
Measurement parameters		
Measurement noise in position, $\sigma_{\text{meas,pos}}$	10	m (1σ)
Measurement noise in velocity, $\sigma_{\text{meas,vel}}$	0.25	m/s (1σ)
Data rate	1	Hz
Debris parameters		
Debris mass	0.2	g
Debris velocity	12	km/s
Momentum enhancement factor [38]	2	— —
Strike direction	[.5774; .5774; .5774]	In inertial frame
Filtering parameters		
Time constant τ (initial, before tuning)	10	s (for FOGM)
Process noise spectral density q (initial)	2e−18	km^2/s^5
Time constant τ (final, after tuning)	1	s
Process noise spectral density q (final)	2.15e−17	km^2/s^5
Measurement noise matrix, $\boldsymbol{R}$	$[\sigma^2_{\text{meas,pos}}\boldsymbol{I}_{3\times3}, \boldsymbol{0}_{3\times3}; \boldsymbol{0}_{3\times3}, \sigma^2_{\text{meas,vel}}\boldsymbol{I}_{3\times3}]$	Measurement units^2
Orbit perturbation parameters		
Coefficient of drag, C_D	2.2	— —
Reference altitude, r_o	Per Table 8-4 of [36]	— —
Atmospheric scale height, H	Per Table 8-4 of [36]	— —
Reference density, ρ_o	Per Table 8-4 of [36]	— —
Area of satellite bus	1	m^2
Area of solar array (tracks sun, area relative to $\hat{\boldsymbol{v}}$ varies)	5	m^2

acceleration that grow with each timestep when used in a filter processing the data in reversed time. To correct this, a mirrored FOGM is used in the backward filter, which decays exponentially as the filter moves backward in time through the dataset, as shown in Eq. (15) and Fig. 8. Implementing this change in the state dynamics and state transition matrix is obtained by setting the time constant τ to be negative. τ is also used in the state process noise covariance matrix, and the objective of this appendix is to rederive the coefficients of this state process noise covariance using the mirrored FOGM model to verify the computation of the state process noise covariance in the backward filter.

First, the FOGM acceleration is integrated twice to establish the acceleration, velocity, and position at $t + \Delta t$. Note that this is the kinematic effect of the process noise only; it does not incorporate system dynamics. For a Keplerian orbit and a short timestep, this approximation is sufficient for characterizing the effect of noise on the state, but if longer timesteps or stronger system dynamics were involved, it should be revisited.

$$\boldsymbol{w}(t+\Delta t) = \boldsymbol{w}(t)e^{\Delta t/\tau} \tag{B1}$$

$$\boldsymbol{v}(t+\Delta t) = \boldsymbol{v}(t) + \boldsymbol{w}(t)\tau(e^{\Delta t/\tau} - 1) \tag{B2}$$

$$\boldsymbol{r}(t+\Delta t) = \boldsymbol{r}(t) + \boldsymbol{v}(t)\Delta t - \boldsymbol{w}(t)\tau\Delta t + \boldsymbol{w}(t)\tau^2(e^{\Delta t/\tau} - 1) \tag{B3}$$

where the constants of integration are solved for by noting that at $\Delta t = 0$, $\boldsymbol{w}(t+\Delta t) = \boldsymbol{w}(t)$, $\boldsymbol{v}(t+\Delta t) = \boldsymbol{v}(t)$, and $\boldsymbol{r}(t+\Delta t) = \boldsymbol{r}(t)$.

Next, form the state transition matrix at $t + \Delta t$ by taking the partial derivatives of these equations with respect to the state. Note that this assumes that Δt is small enough for a first-order Taylor series truncation to be used. The STM is found by

$$\Phi(t+\Delta t, t) = \frac{\partial X(t+\Delta t)}{\partial X(t)} \tag{B4}$$

$$\Phi(t+\Delta t, t) = \begin{bmatrix} \boldsymbol{I}_3 & \Delta t\boldsymbol{I}_3 & [\tau^2(e^{\Delta t/\tau} - 1) - \tau\Delta t]\boldsymbol{I}_3 \\ \boldsymbol{0}_{3\times3} & \boldsymbol{I}_3 & \tau(e^{\Delta t/\tau} - 1)\boldsymbol{I}_3 \\ \boldsymbol{0}_{3\times3} & \boldsymbol{0}_{3\times3} & e^{\Delta t/\tau}\boldsymbol{I}_3 \end{bmatrix} \tag{B5}$$

For convenience, the following definitions are formed from this state transition matrix:

$$\Phi_{12} = \Delta t \tag{B6}$$

$$\Phi_{13} = \tau^2(e^{\Delta t/\tau} - 1) - \tau\Delta t \tag{B7}$$

$$\Phi_{21} = \tau(e^{\Delta t/\tau} - 1) \tag{B8}$$

$$\Phi_{33} = e^{\Delta t/\tau} \tag{B9}$$

This approximation of the state transition matrix is then used to form the integrand for the state process noise covariance matrix. The $\boldsymbol{Q}$ is the power spectral density of the acceleration noise, and it is applied in the orbit frame (radial, tangential, normal). The $\boldsymbol{B}$ matrix maps the orbit frame to inertial frame (so that it can be added to the state vector). Thus,

$$\boldsymbol{Q}_{\text{rtn}} = \begin{bmatrix} q_r & 0 & 0 \\ 0 & q_t & 0 \\ 0 & 0 & q_n \end{bmatrix} \tag{B10}$$

$$\boldsymbol{B} = \begin{bmatrix} \boldsymbol{0}_{3\times3} \\ \boldsymbol{0}_{3\times3} \\ \boldsymbol{M}_{\text{rtn}} \end{bmatrix} \tag{B11}$$

where $\boldsymbol{M}_{\text{rtn}}$ is the direction cosine matrix to map the orbit frame to the inertial frame. For convenience, the following definition of $\tilde{\boldsymbol{Q}}$ is established. Note that this is the $\tilde{\boldsymbol{Q}}$ that is used in Eq. (12).

$$\tilde{\boldsymbol{Q}} = \boldsymbol{M}_{\text{rtn}}\boldsymbol{Q}_{\text{rtn}}\boldsymbol{M}_{\text{rtn}}^T \tag{B12}$$

With these, the integrand of the process noise covariance matrix can be assembled, denoted as $\boldsymbol{N}_i$. Recalling Eq. (11), the integrand is

$$\boldsymbol{N}_i = \boldsymbol{\Phi}(t+\Delta t, \epsilon)\boldsymbol{B}(\epsilon)\boldsymbol{Q}(\epsilon)\boldsymbol{B}^T(\epsilon)\boldsymbol{\Phi}^T(t+\Delta t, \epsilon) \tag{B13}$$

such that

$$\boldsymbol{S}_i = \int_t^{t+\Delta t} \boldsymbol{N}_i \, \mathrm{d}\epsilon \tag{B14}$$

Multiplying this out and approximating $\boldsymbol{N}_i$ for one timestep from t to $t + \Delta t$ reduces to

$$\boldsymbol{N}_i \approx \begin{bmatrix} \Phi_{13}^2\tilde{\boldsymbol{Q}} & \Phi_{13}\Phi_{21}\tilde{\boldsymbol{Q}} & \Phi_{13}\Phi_{33}\tilde{\boldsymbol{Q}} \\ \Phi_{13}\Phi_{21}\tilde{\boldsymbol{Q}} & \Phi_{21}^2\tilde{\boldsymbol{Q}} & \Phi_{33}\Phi_{21}\tilde{\boldsymbol{Q}} \\ \Phi_{13}\Phi_{33}\tilde{\boldsymbol{Q}} & \Phi_{33}\Phi_{21}\tilde{\boldsymbol{Q}} & \Phi_{33}^2\tilde{\boldsymbol{Q}} \end{bmatrix} \tag{B15}$$

For the filter, the Φ coefficients of $\boldsymbol{N}_i$ are multiplied out and then integrated to form the γ coefficients for calculating $\boldsymbol{S}_i$. The constants of integration are found by setting $\gamma = 0$ when $\Delta t = 0$.

$$\Phi_{13}^2 = (-\Delta t\tau - \tau^2 + e^{\Delta t/\tau}\tau^2)^2 \tag{B16}$$

$$\gamma_{rr,\text{bkwd}} = \frac{\Delta t^3\tau^2}{3} + \Delta t^2\tau^3 + \Delta t\tau^4 - 2e^{\Delta t/\tau}\Delta t\tau^4 - \frac{\tau^5}{2} + \frac{1}{2}e^{2\Delta t/\tau}\tau^5 \tag{B17}$$

$$\Phi_{21}^2 = \tau^2\left(\Delta t - 2e^{\Delta t/\tau}\tau + \frac{1}{2}e^{2\Delta t/\tau}\tau\right) \tag{B18}$$

$$\gamma_{vv,\text{bkwd}} = \frac{1}{2}\tau^2(2\Delta t + (3\text{–}4e^{\Delta t/\tau} + e^{2\Delta t/\tau})\tau) \tag{B19}$$

$$\Phi_{33}^2 = e^{2\Delta t/\tau} \tag{B20}$$

$$\gamma_{ww,\text{bkwd}} = -\frac{\tau}{2} + \frac{1}{2}e^{2\Delta t/\tau}\tau \tag{B21}$$

$$\Phi_{13}\Phi_{21} = (-1 + e^{\Delta t/\tau})\tau(-\Delta t\tau - \tau^2 + e^{\Delta t/\tau}\tau^2) \tag{B22}$$

$$\gamma_{rv,\text{bkwd}} = \frac{\Delta t^2\tau^2}{2} + \Delta t\tau^3 - e^{\Delta t/\tau}\Delta t\tau^3 + \frac{\tau^4}{2} - e^{\Delta t/\tau}\tau^4 + \frac{1}{2}e^{2\Delta t/\tau}\tau^4 \tag{B23}$$

$$\Phi_{13}\Phi_{33} = e^{\Delta t/\tau}(-\Delta t\tau - \tau^2 + e^{\Delta t/\tau}\tau^2) \tag{B24}$$

$$\gamma_{rw,\text{bkwd}} = -e^{\Delta t/\tau}\Delta t\tau^2 - \frac{\tau^3}{2} + \frac{1}{2}e^{2\Delta t/\tau}\tau^3 \tag{B25}$$

$$\Phi_{33}\Phi_{21} = e^{\Delta t/\tau}(-1 + e^{\Delta t/\tau})\tau \tag{B26}$$

$$\gamma_{vw,\text{bkwd}} = \frac{1}{2}(-1 + e^{\Delta t/\tau})^2\tau^2 \tag{B27}$$

For the forward filter, the γ coefficients are from Carpenter and D'Souza [28] and are repeated here. Note that these are used in the forward filter for the γ coefficients shown in Eq. (12).

$$\gamma_{rr,\text{fwd}} = \frac{\tau^5}{2}\left\{(1-e^{-2\Delta t/\tau}) + \frac{2\Delta t}{\tau}(1\text{–}2e^{-\Delta t/\tau}) - 2\left(\frac{\Delta t}{\tau}\right)^2 + \frac{2}{3}\left(\frac{\Delta t}{\tau}\right)^3\right\} \tag{B28}$$

$$\gamma_{vv,\text{fwd}} = \frac{\tau^3}{2}\{(1-e^{-2\Delta t/\tau}) - 4(1-e^{-\Delta t/\tau}) + 2\Delta t/\tau\} \tag{B29}$$

$$\gamma_{ww,\text{fwd}} = \frac{\tau}{2}(1-e^{-2\Delta t/\tau}) \tag{B30}$$

$$\gamma_{rv,\text{fwd}} = \frac{\tau^4}{2}\left\{(e^{-2\Delta t/\tau}-1) - 2(e^{-\Delta t/\tau}-1) + \frac{2\Delta t}{\tau}(e^{-\Delta t/\tau}-1) + \left(\frac{\Delta t}{\tau}\right)^2\right\} \tag{B31}$$

$$\gamma_{rw,\text{fwd}} = \frac{\tau^3}{2}\left\{(1-e^{-2\Delta t/\tau}) - \frac{2\Delta t}{\tau}e^{-\Delta t/\tau}\right\} \tag{B32}$$

$$\gamma_{vw,\text{fwd}} = \frac{\tau^2}{2}(1-e^{-\Delta t/\tau})^2 \tag{B33}$$

For the backward filter, the text established that setting the time constant τ to be negative is an effective means to adjust the code to use the mirrored FOGM in the backward filter. For the $\boldsymbol{S}_i$ matrix, $\tilde{\boldsymbol{Q}}$ is not a function of τ, so the question is whether using a negative τ in the forward-filter γ_{fwd} coefficients renders an equivalent result to the γ_{bkwd} coefficients derived above. Comparing Eqs. (B17), (B19), (B21), (B23), (B25), and (B27) to Eqs. (B28–B33) with a negative τ, it does render an equivalent result, so the state process noise covariance calculation can be left intact in the backward filter, and no additional sign changes are required within the γ terms beyond setting τ to be negative.

Acknowledgment

This work was supported by a NASA Space Technology Research Fellowship (NASA Grant 80NSSC18 K1142).

References

[1] "Monthly Number of Objects in Earth Orbit by Object Type," *Orbital Debris Quarterly News*, Vol. 23, Nos. 1–2, 2019, p. 13.

[2] Shell, J., "Optimizing Orbital Debris Monitoring with Optical Telescopes," *Advanced Maui Optical and Space Surveillance Technologies Conference*, Maui Economic Development Board, Maui, HI, Sept. 2010.

[3] Christiansen, E., Lyons, F., Davis, B., and Lear, D., "Reaction of Spacecraft Batteries to Hypervelocity Impact," *Orbital Debris Quarterly News*, Vol. 21, No. 1, Feb. 2017, pp. 7–9.

[4] *Space Debris by the Numbers*, European Space Agency, https://www.esa.int/Our_Activities/Space_Safety/Space_Debris/Space_debris_by_the_numbers [retrieved 3 Jan. 2022].

[5] Cunio, P., Bantel, M., Flewelling, B., Therien, W., Jeffries, M., Montoya, M., Butler, R., and Hendrix, D., "Photometric and Other Analyses of Energetic Events Related to 2017 GEO RSO Anomalies," *Proceedings of the Advanced Maui Optical and Space Surveillance (AMOS) Technologies Conference*, Maui Economic Development Board, Maui, HI, Sept. 2017.

[6] "AMOS-5 Suffers Sudden Onboard Failure, Likely Complete Loss," *Spaceflight101*, Nov. 2015, https://spaceflight101.com/amos-5-suffers-sudden-onboard-failure-likely-complete-loss/.

[7] Henry, C., "SES Loses 12 Transponders on NSS-806 Satellite, Says Impact Is Temporary," *SpaceNews*, July 2017, https://spacenews.com/ses-loses-12-transponders-on-nss-806-satellite-says-impact-is-temporary/.

[8] Clark, S., "Investigators Conclude External Forces Killed an Intelsat Satellite in April," *Spaceflight Now*, July 2019, https://spaceflightnow.com/2019/07/30/investigators-conclude-external-forces-killed-an-intelsat-satellite-in-april/.

[9] Krag, H., Serrano, M., Braun, V., Kuchynka, P., Catania, M., Siminski, J., Schimmerohn, M., Marc, X., Kuijper, D., Shurmer, I., O'Connell, A., Otten, M., Munoz, I., Morales, J., Wermuth, M., and McKissock, D., "A 1 cm Space Debris Impact onto the Sentinel-1A Solar Array," *Acta Astronautica*, Vol. 137, Aug. 2017, pp. 434–443. https://doi.org/10.1016/j.actaastro.2017.05.010

[10] Williams, T., Sedlak, J., and Shulman, S., "Magnetospheric Multiscale Mission Micrometeoroid/Orbital Debris Impacts," *Spacecraft Anomalies and Failures Workshop 2017*, NASA and NRO, organized by Dr. Darren McKnight, Dec. 2017.

[11] Graham, G., McBride, N., Kearlsey, A., Drolshagen, G., Green, S., McDonnell, J. A. M., Grady, M., and Wright, I., "The Chemistry of Micrometeoroid and Space Debris Remnants Captured on Hubble Space Telescope Solar Cells," *International Journal of Impact Engineering*, Vol. 26, Nos. 1–10, 2001, pp. 263–274.

[12] Squire, M., "Micrometeoroid and Orbital Debris Testing on Composite Overwrapped Pressure Vessels," *2019 Applied Space Environments Conference*, NASA, May 2019, https://www.hou.usra.edu/meetings/ASEC2019/program/.

[13] "Evaluation of Micrometeoroid and Orbital Debris (MMOD) Risk Predictions with Available On-orbit Assets," NASA NESC-RP-14-01000, NASA Engineering and Safety Center, Oct. 2017.

[14] Flewelling, B., Hendrix, D., Bantel, M., Cunio, P., Therien, W., Jeffries, M., and Clark, C., "Explained and Unexplained Momentum Impulse Transfer Events," *7th European Conference on Space Debris*, ESA Space Debris Office, Darmstadt, Germany, April 2017, Paper 720, https://conference.sdo.esoc.esa.int/proceedings/packages.

[15] Putzar, R., Watson, E., Schimmerohn, M., Karrang, P., and Millinger, M., "How Hypervelocity Impacts Can Affect the LISA Mission—The MIRAD Study," *International Astronautical Congress*, International Astronautical Federation, Paris, France, Oct. 2019.

[16] Thorpe, J. I., Slutsky, J., Baker, J., Littenberg, T., Hourihane, S., Pagane, N., Pokorny, P., Janches, D., Armano, M., Audley, H., et al., "Micrometeoroid Events in LISA Pathfinder," *Astrophysical Journal*, Vol. 883, No. 1, 2019, p. 53.

[17] Williamsen, J., Pechkis, D., Balakrishnan, A., and Ouellette, S., "Characterizing the Orbital Debris Environment Using Satellite Perturbation Anomaly Data," *First International Orbit Debris Conference*, NASA Orbital Debris Program Office, Dec. 2019, Paper 6065.

[18] Bennett, A. A., Schaub, H., and Carpenter, R., "Assessing Debris Strikes in Spacecraft Telemetry: Development and Comparison of Various Techniques," *70th International Astronautical Congress*, International Astronautical Federation, Paris, France, Oct. 2019.

[19] Bennett, A. A., and Schaub, H., "Identifying and Assessing Debris Strikes in NASA Spacecraft Telemetry," *First International Orbital Debris Conference*, NASA Orbital Debris Program Office, Dec. 2019, Paper 6014.

[20] Wright, J., "Orbit Determination Toolkit Theory & Algorithms," Analytical Graphics, Inc., Sept. 2020, https://www.agi.com/resources/whitepapers/orbit-determination-tool-kit-theory-and-algorithms.

[21] Ko, H. C., and Scheeres, D. J., "Maneuver Detection with Event Representation Using Thrust Fourier Coefficients," *Journal of Guidance, Control, and Dynamics*, Vol. 39, No. 5, May 2016, pp. 1080–1091. https://doi.org/10.2514/1.G001463

[22] Holzinger, M. J., Scheeres, D. J., and Alfriend, K. T., "Object Correlation, Maneuver Detection, and Characterization Using Control Distance Metrics," *Journal of Guidance, Control, and Dynamics*, Vol. 35, No. 4, 2012, pp. 1312–1325. https://doi.org/10.2514/1.53245

[23] Kelecy, T., and Jah, M., "Detection and Orbit Determination of a Satellite Executing Low Thrust Maneuvers," *Acta Astronautica*, Vol. 66, Nos. 5–6, 2010, pp. 798–809. https://doi.org/10.1016/j.actaastro.2009.08.029

[24] Jiang, Y., Yang, H., Baoyin, H., and Ma, P., "Extended Kalman Filter with Input Detection and Estimation for Tracking Manoeuvring Satellites," *Journal of Navigation*, Vol. 72, No. 3, 2019, pp. 628–648. https://doi.org/10.1017/S037346331800098X

[25] Watson, E., and Steinhauser, M., "Discrete Particle Method for Simulating Hypervelocity Impact Phenomena," *Materials*, Vol. 10, No. 4, 2017, p. 379. https://doi.org/10.3390/ma10040379

[26] Williamsen, J., Pechkis, D., Balakrishnan, A., and Ouellette, S., "Characterizing the Orbital Debris Environment Using Satellite Perturbation Anomaly Data," IDA Document NS D-10643. Inst. for Defense Analyses, June 2019.

[27] Tapley, B. D., Schutz, B. E., and Born, G. H., *Statistical Orbit Determination*, Elsevier/Academic Press, Amsterdam, 2004, p. 212.

[28] Carpenter, R., and D'Souza, C., "Navigation Filter Best Practices," NASA TP 2018-219822, April 2018.
[29] Lear, W., "Kalman Filtering Techniques," NASA Johnson Space Center Rept. JSC-20688, Houston, TX, 1985.
[30] Fraser, D., "A New Technique for the Optimal Smoothing of Data," Ph.D. Thesis, Massachusetts Inst. of Technology, Cambridge, MA, Jan. 1967.
[31] Fraser, D., and Potter, J., "The Optimum Linear Smoother as a Combination of Two Optimum Linear Filters," *IEEE Transactions on Automatic Control*, Vol. 14, No. 4, 1969, pp. 387–390. https://doi.org/10.1109/TAC.1969.1099196
[32] Brown, R. G., and Hwang, P. Y. C., *Introduction to Random Signals and Applied Kalman Filtering: With MATLAB Exercises*, 4th ed., Wiley, Hoboken, NJ, 2012, Chap. 6.
[33] "NASA Orbital Debris Engineering Model ORDEM 3.1–Software User Guide," Dec. 2019, https://ntrs.nasa.gov/api/citations/20190033393/downloads/20190033393.pdf.
[34] Moulin, P., and Veeravalli, V. V., *Statistical Inference for Engineers and Data Scientists*, Cambridge Univ. Press, New York, 2019.
[35] Squire, M., "Evaluating Micrometeoroid and Orbital Debris Risk Assessments Using Anomaly Data," NASA Langley Research Center, https://ntrs.nasa.gov/api/citations/20170010258/downloads/20170010258.pdf.
[36] Vallado, D. A., and McClain, W. D., *Fundamentals of Astrodynamics and Applications*, 4th ed., Space Technology Library 21, Microcosm Press, Hawthorne, CA, 2013, Chap. 8.
[37] Schaub, H., and Junkins, J. L., Analytical Mechanics of Space Systems, 3rd ed., AIAA Education Series, AIAA, Reston, VA, 2014, Chap. 11.
[38] Williamsen, J., and Evans, S., "Orbital Debris Momentum Transfer in Satellite Shields Following Hypervelocity Impact, and Its Application to Environment Validation," *Procedia Engineering*, Vol. 204, 2017, pp. 500–507. https://doi.org/10.1016/j.proeng.2017.09.747

O. L. de Weck
Associate Editor